

See discussions, stats, and author profiles for this publication at: <https://www.researchgate.net/publication/303486235>

OceanModelling2016

Dataset · May 2016

READS

65

7 authors, including:



Ning Li

University of Hawai'i System

12 PUBLICATIONS 48 CITATIONS

[SEE PROFILE](#)



Kwok Fai Cheung

University of Hawai'i at Mānoa

131 PUBLICATIONS 2,527 CITATIONS

[SEE PROFILE](#)



Justin E. Stopa

Institut Français de Recherche pour l'Explo...

22 PUBLICATIONS 191 CITATIONS

[SEE PROFILE](#)

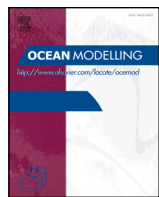


Yi-Leng Chen

University of Hawai'i at Mānoa

90 PUBLICATIONS 1,850 CITATIONS

[SEE PROFILE](#)



Thirty-four years of Hawaii wave hindcast from downscaling of climate forecast system reanalysis

Ning Li^a, Kwok Fai Cheung^{a,*}, Justin E. Stopa^b, Feng Hsiao^c, Yi-Leng Chen^c, Luis Vega^d, Patrick Cross^d

^a Department of Ocean and Resources Engineering, University of Hawaii, Honolulu, HI 96822, USA

^b Laboratory of Ocean Physics and Satellite Oceanography, University of Brest, Plouzane, France

^c Department of Atmospheric Sciences, University of Hawaii, Honolulu, HI 96822, USA

^d Hawaii Natural Energy Institute, University of Hawaii, Honolulu, HI 96822, USA

ARTICLE INFO

Article history:

Received 15 September 2015

Revised 5 January 2016

Accepted 1 February 2016

Available online 10 February 2016

Keywords:

Swells

Wind waves

Wave hindcast

Island sheltering

Spectral wave models

Weather Research and Forecasting model

ABSTRACT

The complex wave climate of Hawaii includes a mix of seasonal swells and wind waves from all directions across the Pacific. Numerical hindcasting from surface winds provides essential space-time information to complement buoy and satellite observations for studies of the marine environment. We utilize WAVEWATCH III and SWAN (Simulating WAves Nearshore) in a nested grid system to model basin-wide processes as well as high-resolution wave conditions around the Hawaiian Islands from 1979 to 2013. The wind forcing includes the Climate Forecast System Reanalysis (CFSR) for the globe and downscaled regional winds from the Weather Research and Forecasting (WRF) model. Long-term in-situ buoy measurements and remotely-sensed wind speeds and wave heights allow thorough assessment of the modeling approach and data products for practical application. The high-resolution WRF winds, which include orographic and land-surface effects, are validated with QuickSCAT observations from 2000 to 2009. The wave hindcast reproduces the spatial patterns of swell and wind wave events detected by altimeters on multiple platforms between 1991 and 2009 as well as the seasonal variations recorded at 16 offshore and nearshore buoys around the Hawaiian Islands from 1979 to 2013. The hindcast captures heightened seas in interisland channels and around prominent headlands, but tends to overestimate the heights of approaching northwest swells and give lower estimates in sheltered areas. The validated high-resolution hindcast sets a baseline for future improvement of spectral wave models.

© 2016 Elsevier Ltd. All rights reserved.

1. Introduction

Hawaii has unique wave climate associated with its North Central Pacific location and massive archipelago. Fig. 1 provides a location map to illustrate the prominent wave regimes and geographical features. Extratropical storms near the Kuril and Aleutian Islands generate swells toward Hawaii from the northwest to north during the boreal winter. The south facing shores experience moderate swells from the year-round Southern Hemisphere Westerlies that are augmented by mid-latitude cyclones in the boreal summer. The persistent trade winds generate waves from the northeast to east throughout the year, while subtropical cyclones during the winter and passing cold fronts can generate waves from all directions. The steep volcanic mountains speed up the wind flows in

the channels and create prominent wakes leeward of the Hawaiian Islands (Yang et al., 2005; Nguyen et al., 2010; Hitzl et al., 2014). These localized wind flows together with island sheltering create regional wave patterns with large spatial and temporal variations (Aucan, 2006; Caldwell et al., 2009; Stopa et al., 2011).

There are increasing demands for long-term wave data in support of ocean renewable energy planning, marine ecosystem assessment, shoreline management, and infrastructure development in Hawaii. Altimeters aboard polar orbiting satellites have the advantage of providing significant wave heights with global expanse. The observations are available along satellite tracks at time intervals between 10 and 35 days. The lack of wave direction and period in a multi-modal sea state as well as contamination of the signals by landmasses hamper their application in coastal regions. Offshore and nearshore buoys have provided in-situ wave measurements at strategic locations along the island chain as shown in Fig. 1. Some of the buoys recorded over 30 years of wave data and most of the recent measurements are directional. Despite their ability to fully record the sea state, they are limited to discrete

* Corresponding author. Tel.: +1 808 956 3485; fax: +1 808 956 3498.

E-mail addresses: ningli@hawaii.edu (N. Li), cheung@hawaii.edu (K.F. Cheung), Justin.Stopa@ifremer.fr (J.E. Stopa), hsiao@hawaii.edu (F. Hsiao), yileng@hawaii.edu (Y.-L. Chen), luisvega@hawaii.edu (L. Vega), pscross@hawaii.edu (P. Cross).

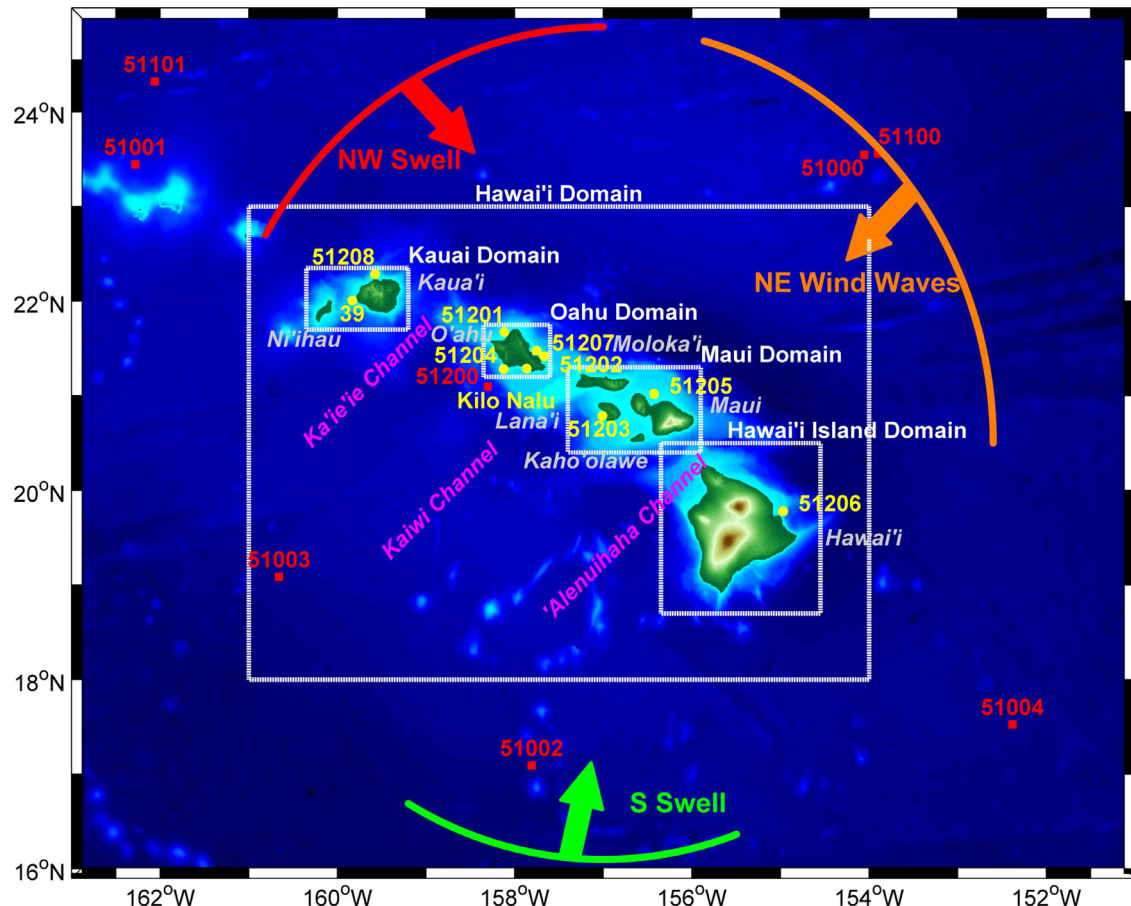


Fig. 1. Illustration of Hawaii wave climate, location map for buoys and geographical features, and layout of nested computational grids for WAVEWATCH III and SWAN.

locations and subject to downtime due to equipment failure and maintenance. A detailed description of the complex wave climate in Hawaii is best accomplished by numerical modeling, while measurements from altimeters and buoys are useful for validation of the model results and assessment of the model performance.

Third generation spectral wave models, such as WAVEWATCH III of Tolman (2008) and SWAN (Simulating WAves Nearshore) of Booij et al. (1999), are proven tools in describing the multi-modal sea states of Hawaii (Stopa et al., 2011). Despite being developed for open oceans and shelf seas, WAVEWATCH III is able to depict shadowing of the wave field by the Hawaiian Islands and heightened seas with small fetches in interisland channels and around headlands (Stopa et al., 2013; Foster et al., 2014). SWAN is better suited for near-shore environments due to its efficient implicit scheme to compute wave processes in fine resolution and ability to account for triad wave interactions in shallow water. Filipot and Cheung (2012) provided additional parameterizations for energy dissipation due to wave breaking and bottom friction in the fringing reef environment of Hawaii. The nesting of WAVEWATCH III and SWAN has proven its effectiveness in modeling wave generation and propagation from the open ocean to the shore.

High-quality global and regional wind forcing is critical for modeling of the multi-modal seas in Hawaii. Reanalysis datasets provide an opportunity to reproduce global wave conditions with high fidelity (Arinaga and Cheung, 2012; Caires et al., 2004; Chawla et al., 2013; Stopa et al., 2013). The Climate Forecast System Reanalysis (CFSR) of NOAA NCEP was generated from a suite of coupled ocean, land, ice, and atmospheric models with assimilation of observations in three space dimensions (Saha et al., 2010). Its products include hourly surface winds on a 0.5° grid from 1979 to 2010.

The same model system produces the CFS version 2 reforecast data with 0.205° resolution from 2011 onward as an extension of CFSR (Saha et al., 2014). The ECMWF Reanalysis (ERA) Interim includes coupling to a spectral wave model and a 4-dimensional assimilation method (Dee et al., 2011). It has surface wind data every 3 h with a ~0.7° grid spacing from 1979 to present. Stopa and Cheung (2014) inter-compared the wind speeds from CFSR and ERA-Interim with altimetry and buoy observations, and concluded that although both products have good spatial homogeneity and consistent levels of errors, CFSR provides better descriptions of the upper percentile winds for wave hindcasting.

The orographically induced airflow over Hawaii waters is not resolved by global reanalysis. The wind flow is significantly modified by steep volcanic mountains of up to 4000 m high and islands of up to 140 km across as well as the diurnal land-sea thermal contrast (Yang et al., 2005; Nguyen et al., 2010; Carlis et al., 2010). High-resolution wind data from locally calibrated atmospheric models is crucial for hindcasting the wave conditions around the Hawaiian Islands (Stopa et al., 2011, 2013). With proper descriptions of lower boundary conditions such as terrain, vegetation cover, and soil type, high-resolution models have considerable skills in simulating the island-scale airflow, weather climate, and ocean surface winds (e.g., Zhang et al., 2005; Yang et al., 2005; Carlis et al., 2010; Nguyen et al., 2010). The Weather Research and Forecasting (WRF) model of Skamarock and Klemp (2008) has become a standard tool for Hawaii regional climate studies (Hitzl et al., 2014). In addition, the high-resolution WRF model was employed for simulation of a heavy rainfall event over Oahu associated with a Kona storm and a winter cold front in the mid-Pacific by Tu and Chen (2011).

Table 1
Nested computational grids for spectral wave and mesoscale atmospheric modeling.

Model	Grid	Longitude	Latitude	Resolution
WAVEWATCH III	Global	180°W–180°E	77.5°S–77.5°N	0.5 arc-degree
WAVEWATCH III	Hawaii	161°W–154°W	18°N–23°N	3 arc-min
SWAN	Kauai	160.35°W–159.2°W	21.7°N–22.35°N	0.3 arc-min
SWAN	Maui	157.4°W–155.9°W	20.4°N–21.3°N	0.3 arc-min
SWAN	Oahu	158.35°W–157.6°W	21.2°N–21.75°N	0.3 arc-min
SWAN	Hawaii Island	156.2°W–154.7°W	18.85°N–20.35°N	0.3 arc-min
WRF	Central Pacific	175.67°W–136.26°W	6.35°N–37.98°N	18 km
WRF	Hawaii	167.22°W–149.30°W	15.39°N–26.69°N	6 km

and Zhou and Chen (2014). The results from these studies were validated against surface maps, sounding data, and surface measurements.

In this paper, we describe a long-term hindcast using WAVEWATCH III and SWAN to characterize the complex wave climate around the Hawaiian Islands for a 34-year period from February 1979 to May 2013. Section 2 summarizes the setup of the spectral wave models in a system of global, regional, and nearshore computational grids. The wind forcing includes CFSR for the entire globe and downscaled WRF winds for the Hawaii region to account for distant swells as well as local contributions to the wind waves. A number of error metrics are defined for assessment of the hindcast against measurements from buoys and satellites. In Section 3, we demonstrate the local climate patterns through examples of typical wind and wave events from the hindcast dataset and satellite measurements. These include waves generated by trade winds, a subtropical cyclone, and a passing cold front as well as a north and a south Pacific swell. Section 4 compares the computed wind and wave data with long-term satellite and buoy observations as well as previous and existing hindcast datasets. This is followed by a summary of the findings in Section 5.

2. Methodology

We build on the methodology of Stopa et al. (2013), who hindcast the wave conditions around the Hawaiian Islands with three levels of nested grids using the Final Global Tropospheric Analysis (FNL) winds for 2000 to 2009. The present model setup involves the same resolution for Hawaii WAVEWATCH III, but higher resolution for global WAVEWATCH III and island-scale SWAN. The earlier study utilized the source term package of Tolman and Chalikov (1996) in WAVEWATCH III version 3.14. There have been advances in the source term development and implementation (Ardhuin et al., 2010; Banner et al., 2010; Bidlot et al., 2007; Leckler et al., 2013; Rascle and Ardhuin, 2013; Roger et al., 2012; Tolman et al., 2013; Zieger et al., 2015). In the present study, we make use of the package of Ardhuin et al. (2010) with updated descriptions of non-linear swell dissipation, wave breaking, and wind stress in WAVEWATCH III version 4.18 (Tolman et al., 2014). The island-scale wave processes are modeled using the source term of Van der Westhuyzen (2007) and Van der Westhuyzen et al. (2007) in SWAN version 40.81, which was modified to include the parameterizations developed by Filipot and Cheung (2012) for tropical island environments. CFSR, which has improved physics, assimilation, and resolution compared to FNL, provides the boundary conditions for Hawaii WRF. This results in more accurate global and regional wind forcing for the wave models over a longer period from 1979 to 2013. Additional measurements from multiple altimeters and recently deployed near-shore buoys allow for more thorough assessment of the wave hindcast around the Hawaiian Islands.

2.1. Model setup

We utilize a system of nested global, regional, and island-scale spectral wave models to capture physical processes at increasing

temporal and spatial resolution. Table 1 lists the coverage and resolution of each computational grid. The global WAVEWATCH III model, which resolves the oceans from 77.5°S to 77.5°N at 0.5° (~55 km near Hawaii), has a two-way nested regional grid covering the major Hawaiian Islands at 3 arc-min (~5.5 km) resolution. The finer regional grid is needed to describe the wave field in the shadows of the islands (Ponce de Leon and Guedes Soares, 2005; Stopa et al., 2011). The regional WAVEWATCH III provides directional wave spectra along the boundaries of the nested SWAN grids around Oahu, Kauai, Maui and Hawaii Island for modeling of coastal wave transformation with 18 arc-sec (~550 m) resolution. The multimodal wave conditions are resolved with 50 logarithmic frequency bins and 36 constant directional bins. Fig. 1 illustrates the setup of the island-scale nested grids within the Hawaii regional domain. The island-scale SWAN describes wave transformation over the insular shelf and around headlands, where high-quality bathymetry comes from a blended multibeam and LiDAR dataset (Cheung et al., 2013). The results may in turn define the boundary conditions for higher-resolution computations of the wave conditions at the shore using phase-averaged or phase-resolving models (Li et al., 2014).

The wind forcing for the wave hindcast comes from CFSR for the entire globe and downscaled WRF winds for the Hawaii region. The global wind dataset was generated from a suite of coupled models that includes the Global Forecast System of Yang et al. (2006), the Modular Ocean Model (MOM) version 4 and sea ice model from the Geophysical Fluid Dynamic Laboratory (Griffies et al. 2004), and the NOAH Land Surface Model of Ek et al. (2003) with assimilation of ground-based, aircraft, ship, and satellite observations (Saha et al., 2010, 2014). The atmospheric model has 64 vertical layers extending from the surface to 0.2 hPa on a 0.5° (~55 km) grid from 1979 to 2010 and a 0.205° (~22.5 km) grid from 2011 onward. The output defines the initial and boundary conditions for Hawaii WRF, which is based on a two-way nested grid system with 38 vertical sigma levels from the surface to 100 hPa (Hitzl et al., 2014). Table 1 includes the horizontal coverage and resolution of the computational grids. The level-1 grid covers the North Central Pacific at 18 km resolution to accurately model the synoptic weather. It also provides a transition to the level-2 grid, which resolves the mesoscale wind flows around the Hawaiian Islands at 6 km resolution. The NOAH Land Surface Model accounts for vegetation coverage and land surface properties of the Hawaiian Islands using data compiled by Zhang et al. (2005).

The large computational and storage requirements of the 34-year hindcast call for a careful data management scheme. The pressure, temperature, moisture, and wind velocity from CFSR are interpolated in space and time to define the initial and boundary conditions for Hawaii WRF. The production consists of a series of overlapping 36-h daily runs with the wind velocity output at the standard 10 m elevation every hour. The first 12 h allow for model spin-up and the output from the remaining 24 h is concatenated to produce a continuous 34-year dataset. The hourly WRF wind data around the Hawaiian Islands and the CFSR winds for the entire globe are then interpolated in space and time to define the forcing

Table 2

Locations and temporal coverage of offshore and nearshore buoys used in model validation.

Buoy	Computational grid	Latitude (°N)	Longitude (°W)	Depth (m)	Temporal coverage
51000	Global WAVEWATCH III	23.546	154.056	4275	2009.4–2013.3
51001	Global WAVEWATCH III	23.445	162.279	3430	1981.2–2009.12
51002	Global WAVEWATCH III	17.094	157.808	5002	1984.9–2013.1
51003	Hawaii WAVEWATCH III	19.018	160.582	4919	1984.11–2013.6
51004	Global WAVEWATCH III	17.602	152.395	5230	1984.11–2013.6
51100	Global WAVEWATCH III	23.558	153.900	4755	2009.4–2013.6
51101	Global WAVEWATCH III	24.321	162.058	4792	2008.2–2013.6
51201	Oahu SWAN	21.669	158.120	200	2001.12–2013.6
51202	Oahu SWAN	21.414	157.679	82	2000.8–2013.6
51204	Oahu SWAN	21.281	158.124	302	2010.10–2013.6
51207	Oahu SWAN	21.4775	157.7526	81	2012.10–2013.6
KNOH1	Oahu SWAN	21.288	157.865	12	2008.9–2012.1
39	Kauai SWAN	22.00667	159.8333	110	1982.10–1993.9
51203	Maui SWAN	20.78778	157.0098	201	2007.5–2013.6
51205	Maui SWAN	21.0195	156.4272	193	2011.12–2013.6
51206	Hawaii Island SWAN	19.78143	154.968	347	2012.3–present

for wave modeling. The nested global and Hawaii WAVEWATCH III hindcast comprises 34 overlapping 12.5-month runs with the first half month for model spin-up and the remaining 12 months for archiving. Parameters such as significant wave heights, peak periods, and peak directions of the spectral partitions are archived at all grid points. Two-dimensional wave spectra are only output at buoy locations at hourly intervals and along boundaries of the four island-scale domains for non-stationary SWAN computation. The nesting of SWAN in WAVEWATCH III produces higher resolution wave conditions over the shallow insular shelves and reefs for model validation. The setup also provides a framework for subsequent modeling of the nearshore wave conditions from the archived spectral boundary conditions.

2.2. Observational data

QuikSCAT provided wind measurements over 90% of the ice-free ocean surface daily from 1999 to 2009. An onboard scatterometer pulsed cloud-penetrating microwaves in the Ku band toward the earth and recorded the backscatter signals under a majority of weather conditions. The wind speed and direction at 10-m elevation are estimated from the backscattered signals using the Geophysical Model Function along with the Direction Interval Retrieval with Threshold Nudging method (Ebuchi et al., 2002). The polar orbiting satellite flew over Hawaii in ascending and descending passes. The observations over the 1800-km swath, which covers most of the island chain, have been post-processed into a spatial grid of approximately 12.5 km resolution to capture mesoscale wind features (JPL, 2000). The dataset excludes land, coastal, and sea ice regions and provides rain information for users to remove potentially contaminated data. The post-processed QuikSCAT winds provide a comparison with interpolated data from the Hawaii WRF model.

Significant wave heights detected by actively emitting Ku-microwave signals of satellite altimeters are instrumental for wave model validation and development (Raschke and Ardhuin, 2013; Stora et al., 2015; Ardhuin et al., 2010). Once the measured wave heights are quality controlled and corrected for sensor biases, their accuracy is comparable to buoy measurements with the advantage of global coverage (Zieger et al., 2009). The GlobWAVE project under the European Space Agency compiled a comprehensive dataset from multiple platforms (Queffeuilou and Croize-Fillon, 2010). The data sources include European Remote Sensing 1 (1991–1996) and 2 (1995–2003), Environmental Satellite (2002–2012), Jason 1 (2001–2013) and 2 (2008–present), Topex-Poseidon (1992–2005), and GEOSAT Follow-on (1998–2008). The GlobWAVE

dataset only includes measurements with strong signal to noise ratio and free from anomalous objects and landmasses. The standard error is approximately 0.1 m, or 10% of the significant wave height whichever is larger. The merged along-track measurements cover most of the Hawaii region from 1991 to 2011 for wave model validation.

Hawaii has extensive wave records from a number of buoys for evaluation and validation of the 34-year hindcast. Table 2 lists the coordinates, water depths, and data periods of 7 offshore and 9 nearshore buoys considered in this study. We use National Data Buoy Center (NDBC) numbers to identify the buoys except for Barking Sands, which only has a Coastal Data Information Program (CDIP) number. The offshore buoys #51001, 51003, 51002, 51004, 51100, 51000, and 51101 around the Hawaiian Island chain have 5–30 years of records and provide general wave conditions for the validation of the WAVEWATCH III hindcast. Additional wave measurements are available from nearshore buoys: #39 off west Kauai; #51201, 51202, 51204, and 51207 around Oahu; #51203 and 51205 off west and north Maui; and #51206 off east Hawaii Island (see Fig. 1 for location map). Coastal wave measurements are available from KNOH1, which is a bottom pressure sensor at 12 m water atop a fringing reef on the south shore of Oahu. Most of the nearshore buoys were deployed after 2010 as part of the Pacific Islands Ocean Observing System. They detect wave conditions simultaneously on the open and lee sides of an island or island group for validation of the SWAN results and examination of the model capability in describing wave conditions around the islands.

2.3. Error metrics

The recorded and hindcast datasets have different spatial and temporary resolutions. We post-process the hindcast data to match the record location and time stamp and compile data pair sequences for direct comparison. A number of error metrics available to measure the difference between the two datasets. These include the mean error or bias and the root-mean-square error, defined as

$$ME = \frac{1}{n} \sum_{i=1}^n (y_i - x_i) \quad (1)$$

$$RMSE = \sqrt{\frac{1}{n} \sum_{i=1}^n (y_i - x_i)^2} \quad (2)$$

where (x_i, y_i) denote the recorded and hindcast data pairs and n is the number of data pairs. The overall agreement can be illustrated

by the correlation coefficient and scatter index as

$$\text{COR} = \frac{\sum_{i=1}^n (y_i - \bar{y})(x_i - \bar{x})}{\sqrt{\sum_{i=1}^n (y_i - \bar{y})^2} \sqrt{\sum_{i=1}^n (x_i - \bar{x})^2}} \quad (3)$$

$$\text{SI} = \frac{1}{\bar{x}} \sqrt{\frac{1}{n} \sum_{i=1}^n [(y_i - \bar{y}) - (x_i - \bar{x})]^2} \quad (4)$$

where the over bar indicates time average.

A scatter plot of the data pairs can illustrate the general relationship between the records and hindcast to complement the error matrices. A regression line can provide additional insight by

showing the variation of the bias over the data range. The time lag between recorded and hindcast events might contribute to the scatter of the data even with good agreement of the magnitude. We use the quantile–quantile (Q–Q) plots to compare the percentile distributions of the two datasets independent of the time stamps. It should be noted that the records also contain errors and are only used as a reference for comparison.

3. Hawaii wave climate

Hawaii experiences persistent trade winds and episodic cold fronts throughout the year, as well as occasional subtropical

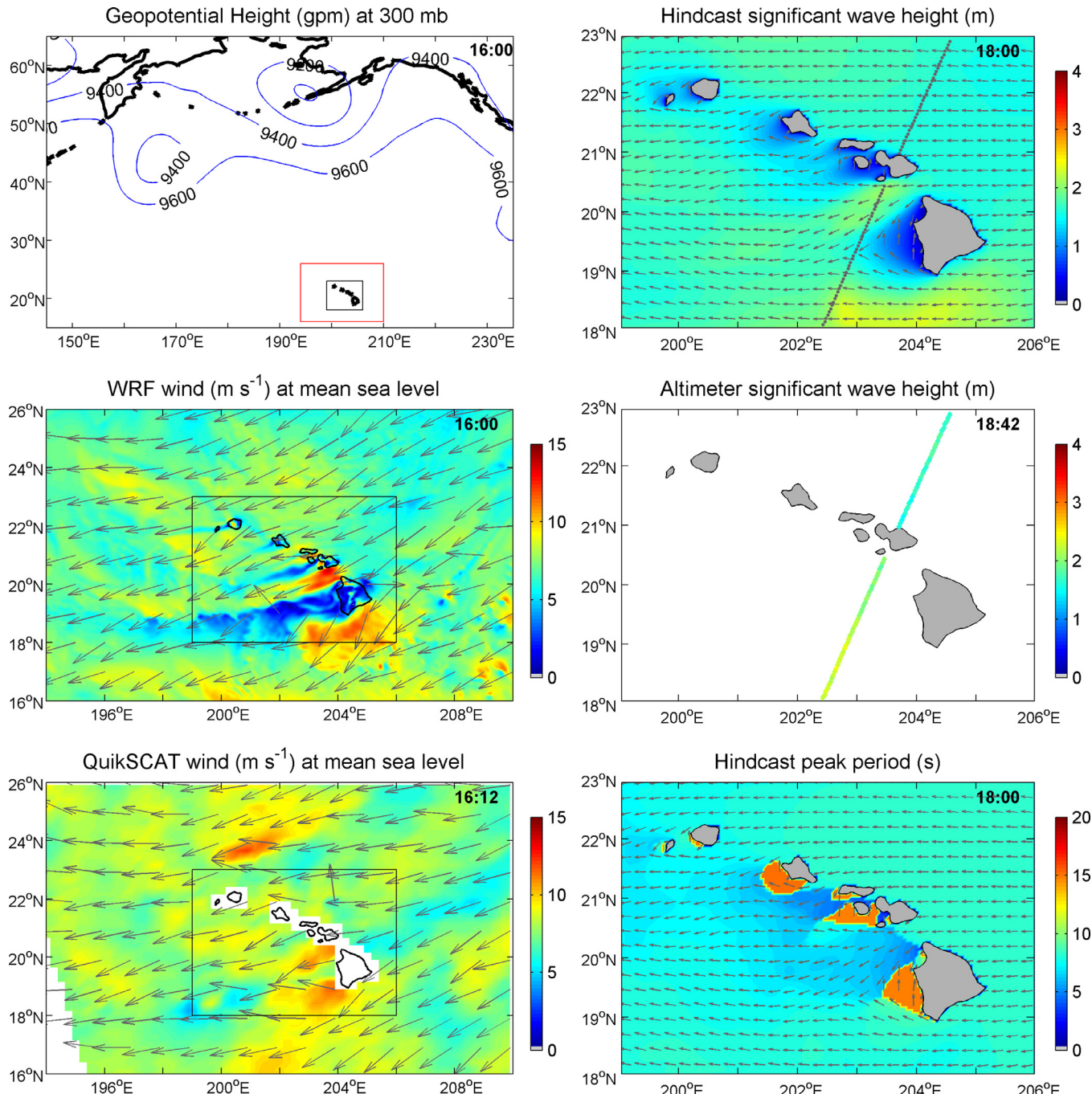


Fig. 2. Meteorological and wave conditions from models and satellites for the trade wind event on August 17, 2005. The red and black boxes in the left panels outline the high-resolution WRF and WATCHWATCH III domains. (For interpretation of the references to color in this figure legend, the reader is referred to the web version of this article.)

cyclones in the winter months. These events generate wind waves with 6–12 s period that are mixed with long-period swells from north and south Pacific extratropical cyclones. An understanding of the underlying processes and local features is necessary to identify the strengths and weaknesses of the hindcast. Although the sea state is typically multi-modal, we select representative wind wave and swell events from the 34-year dataset to illustrate the Hawaii regional wind and wave climate. Satellite observations allow assessment of the hindcast in capturing the selected events as well as their spatial patterns introduced by the island chain.

Trade wind waves are the most common, especially during the summer months, when the subtropical high to the north of Hawaii is strong and stable. Fig. 2 shows a typical trade wind and wave

event on 17 August, 2005. The geopotential height at 300 mbar indicates the presence of a subtropical high-pressure to the north of Hawaii setting up a regime of persistent trade winds toward the islands. Hawaii WRF and QuikSCAT at the nearest time stamp show trade winds of 5–7 m s⁻¹ from the northeast as well as deceleration in front of the islands and acceleration in channels and around southern Hawaii Island. WRF produces more refined features of the wind field especially in the wake of Hawaii Island. QuikSCAT cannot fully capture these small-scale processes with a spatial resolution of ~12.5 km. The trade winds generate waves with 1.5 m significant wave height and 8 s peak period from the east. The acceleration of the trade winds in the channels and south of Hawaii Island augments the local wave height to 2.2 m. The altimeter

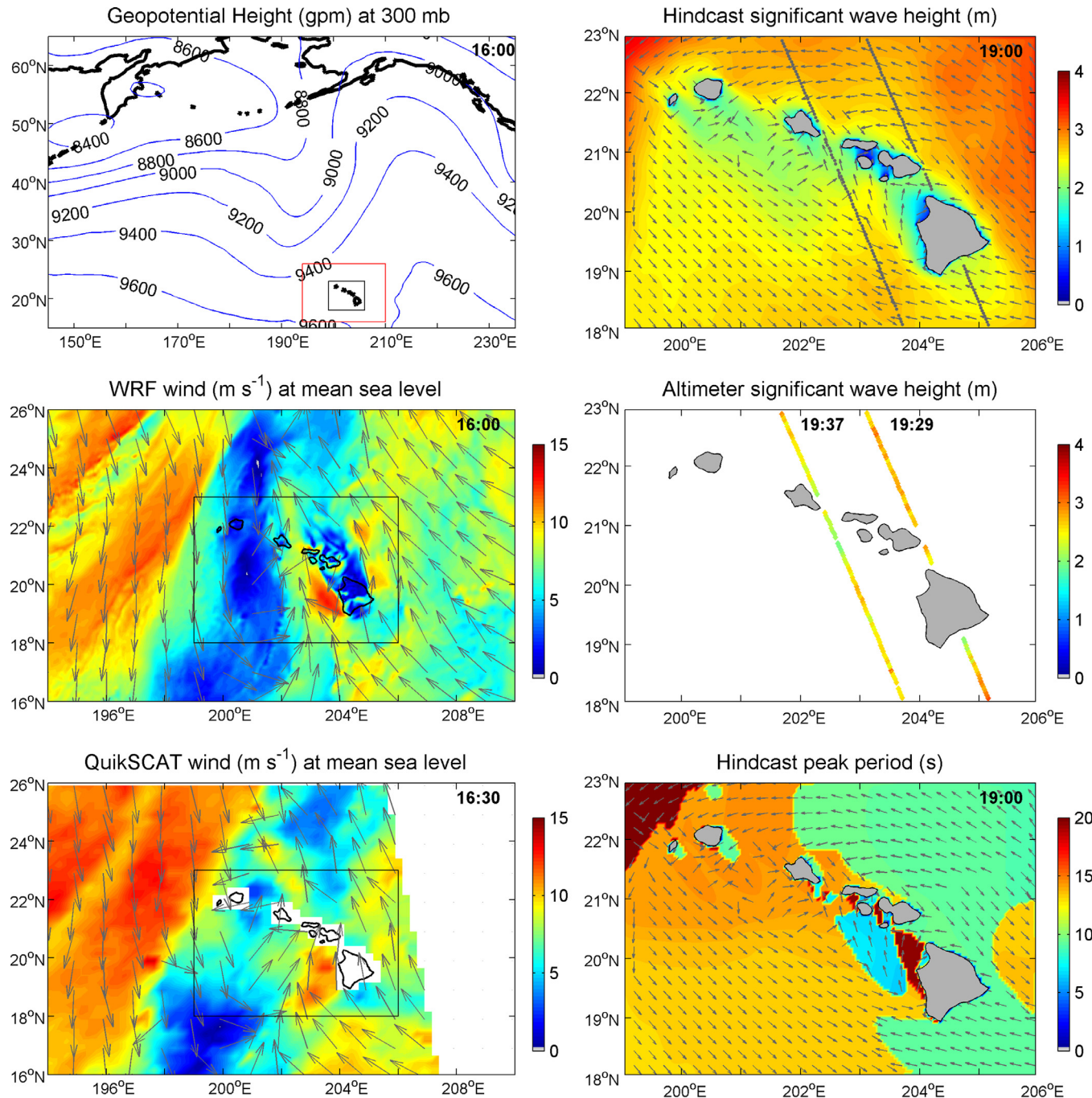


Fig. 3. Meteorological and wave conditions from models and satellites for the cold front on March 1, 2004. The red and black boxes in the left panels outline the high-resolution WRF and WATCHWATCH III domains. (For interpretation of the references to color in this figure legend, the reader is referred to the web version of this article.)

observation from GlobWAVE at the nearest time stamp validates the approaching wave heights as well as the heightened seas associated with local acceleration of the winds. Shadows of the wind waves develop leeward of the islands and expose a long-period south swell of less than 1 m wave height in the background.

The local trade wind flow is occasionally interrupted by cold fronts passing through the Hawaiian Islands from the west to east over a period of several days. Fig. 3 shows the atmospheric and wave conditions when a cold front approached Hawaii on March 1, 2004. The 300-mbar geopotential height indicates a migrating trough to the northwest of Hawaii. Under these synoptic weather conditions, a low-level cyclonic flow is generated

over Kauai and Oahu as seen in the QuikSCAT and WRF wind fields (half an hour apart). The winds transition from 15 m s^{-1} northerly to under 10 m s^{-1} southeasterly across the island chain. The simulated southeasterly winds produce wakes off the north-facing shores of Maui and Hawaii Island with speed under 3 m s^{-1} . QuikSCAT detects the reduction of the wind speed but cannot resolve the detailed airflow in the wakes. The migrating cold front generates northwest waves across the ocean reaching Hawaii with 2.5 m height and 13–14 s period that are evident south of the island chain. These together with locally generated southeast waves and trade wind waves from the far field produce a multi-modal sea state with 3 m wave height and 9 s period to the north. In

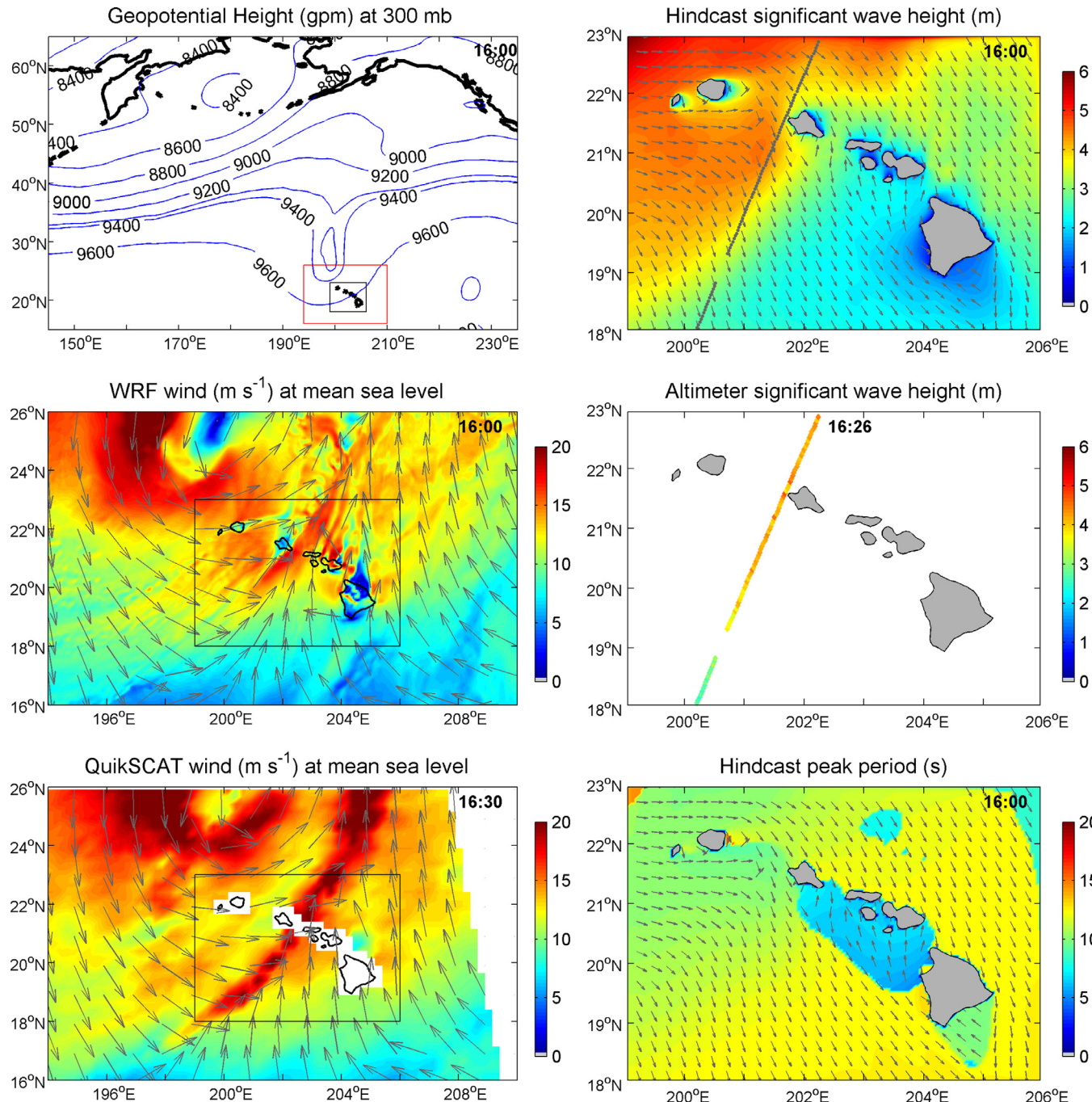


Fig. 4. Meteorological and wave conditions from models and satellites for the Kona storm on Dec 5, 2007. The red and black boxes in the left panels outline the high-resolution WRF and WATCHWATCH III domains. (For interpretation of the references to color in this figure legend, the reader is referred to the web version of this article.)

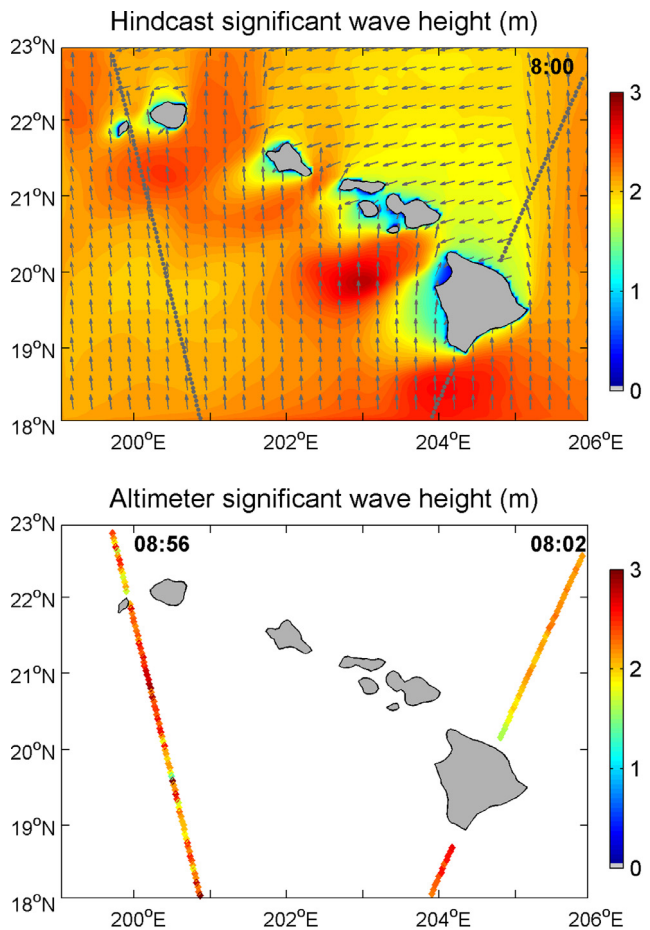


Fig. 5. Wave conditions from models and satellites for the south swell on July 12, 2001.

comparison with the altimetry data, the hindcast reasonably describes the wave height increase from south to north across the island chain as well as sheltering effects southwest of Maui and southeast of Hawaii Island.

Some of the migrating upper-level troughs may develop into subtropical cyclones known locally as “Kona Storms” during the winter ([Simpson 1952](#)). Once developed, a Kona storm moves erratically and can generate winds toward Hawaii from any direction. There are, on average, two to three Kona storms per year ([Otkin and Martin, 2004](#)). [Fig. 4](#) shows a selected event, which occurred on December 5, 2007, for illustration. The 300-mbar geopotential height indicates a trough axis with closed contours north of Kauai that generates a Kona storm over the North Central Pacific.

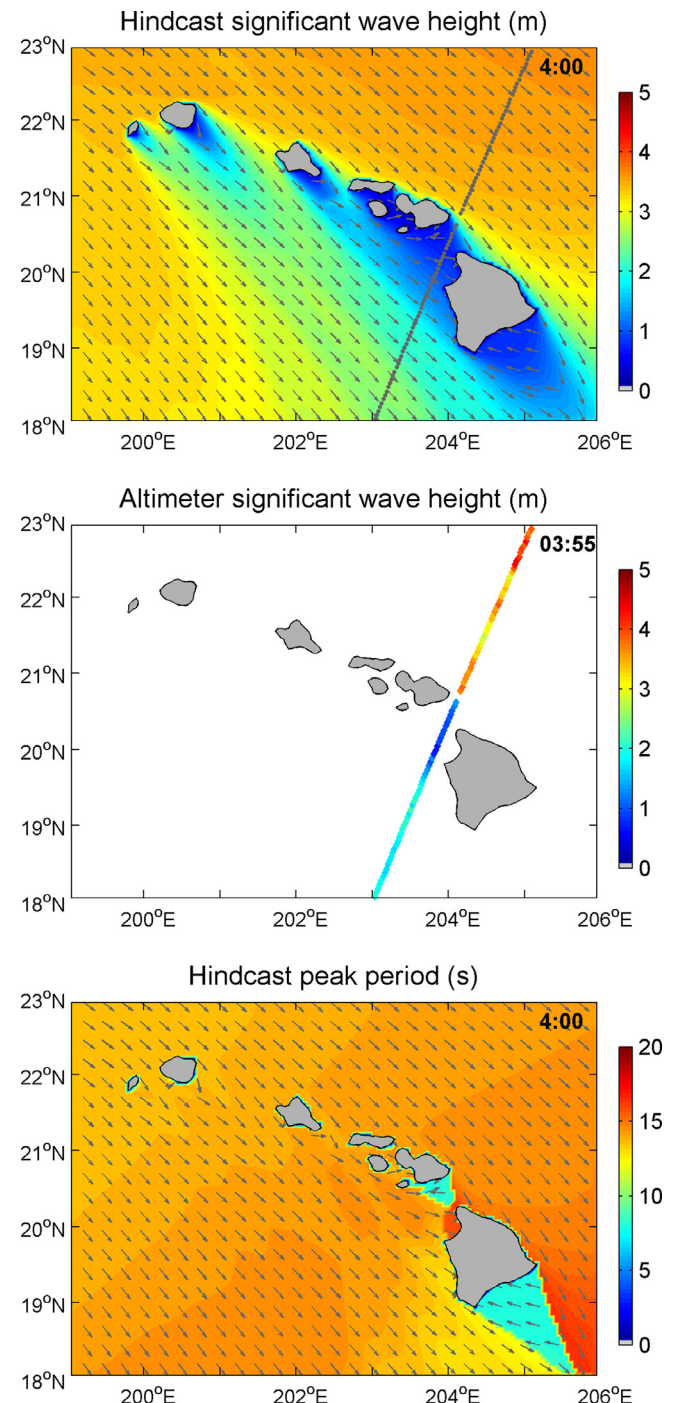


Fig. 6. Wave conditions from models and satellites for the north swell on January 5, 2001.

Both the QuikSCAT and WRF winds resolve the low-level circulations associated with the Kona storm and a strong converging flow across Oahu and Maui on its southeastern flank. The waves reach 6 m height and 10 s period within the core and attenuate toward the east and south following the tail of a northwest swell passing through the islands. Locally generated short-period waves from the converging flow are evident to the south of Maui and Oahu, which are in the shadow of the swell. The altimeter captured a cross section of the storm waves and swell with heights corroborating the hindcast results. The erratic motions of Kona storms can generate severe wave conditions on coastlines that are typically sheltered from trade winds and swells. For infrastructure planning and

development, these events must be taken into consideration as they might produce more severe waves for a given coastline.

In addition to waves associated with local weather, Hawaii also experiences large swells generated by North Pacific extratropical cyclones during the winter months and moderate swells from the South Pacific throughout the year. Fig. 5 provides an illustration of a south swell mixed with east wind waves on July 12, 2001. The approaching swell with 2.1 m significant wave height and 15 s peak period produces shadows north of the island chain, where trade wind waves with 1.8 m height and 7.6 s period are evident. The multimodal sea state is augmented by the heightened wind waves downstream of the channels and around southern Hawaii Island. The altimetry measurements validate the heights of the computed south swell and wind waves and confirm the heightened conditions south of the islands as well as the shadows immediately to the north. Comparing to the south swells, the north Pacific swells approaching Hawaii are more energetic. The direction, which is typically from the northwest, switches to the north at the end of the winter season. Fig. 6 illustrates a prominent shadow along the Hawaiian Islands created by a northwest swell on January 5, 2001. The swell with 3.5 m significant wave height and 15 s peak period is dominant north of the islands. Background wind waves can be seen in the shadows southeast of Hawaii Island and at the Alenuihāhā Channel. In comparison with the altimetry measurements, the hindcast reproduces the swell to the north of the islands as well as the wave height variation in the shadow to the south.

The five case studies have illustrated the typical components of Hawaii's wave climate. Empirical orthogonal function (EOF) analysis of the CFSR wind and wave datasets has shown strong dependence of the swells and trade wind waves on the El Niño Southern Oscillation (Stopa and Cheung, 2014). El Niño years usually have increasing frequency and intensity of north swells (Aucan, 2006), but weaker trade winds and reduced Kona storm activity (Caruso and Businger, 2006; McPhaden et al., 2006). In addition to interannual climate cycles, the wind waves and swells in Hawaii are influenced by long-term climate change. Fyfe (2003) and Yin (2005) showed polarward intensification of the extratropical cyclones in the Southern and Northern Hemispheres in recent decades and into the 21st century. O'Connor and Chu (2015) showed 44% decrease of Kona Lows and 23% decrease of cold fronts for the La Niña years from the 1956–1982 to the 1983–2010 epoch. The buoy records from around Hawaii indicate shifting of trade winds from northeast to east during the 1980s–000 epoch (Garza et al., 2012). Through satellite and buoy records, reanalysis datasets, and model simulations, Boisséson et al. (2014) showed robust strengthening of trades winds over the Pacific during the past 20 years. The swells and wind waves reflect the changing extratropical cyclone, local storm and trade wind patterns. After validation with available observations, the 34-year high-resolution hindcast provides a wealth of information for studies of interannual cycles and long-term climate change as well as their impact to Hawaii.

4. Assessment of hindcast

We have illustrated the spatial patterns of typical wind and wave events around the Hawaiian Islands. The main features include heightened winds and waves in channels and around southern Hawaii Island as well as relatively calm conditions on the lee side of the islands. The selected events qualitatively demonstrate the capability of the hindcast in describing the complex sea states, which have significant implications for the marine environment and coastal infrastructure. With the typical spatial patterns identified, we now provide quantitative assessment and validation of the 34-year hindcast dataset in terms of the error metrics against long-term satellite and buoy measurements.

4.1. Validation with satellite data

Satellite observations allow validation of the complex spatial patterns of the hindcast around the Hawaiian Islands. The year-round trade winds have seasonal patterns influenced by the location of the subtropical high north of Hawaii. Fig. 7 compares the average surface winds from WRF and QuikSCAT in the summer months of June, July and August and the winter months of December, January, and February during 2000 to 2009. The subtropical high is directly northeast of Hawaii in the summer. WRF shows average trades of $6\text{--}8 \text{ m s}^{-1}$ from the east-northeast with maximum reaching 11 m s^{-1} in the Alenuihāhā Channel and relatively calm conditions in the wake of Hawaii Island. The subtropical high migrates toward the northeast Pacific in the winter. The trade winds weaken and shift to a more easterly direction. The more compact winds have an average speed of $3\text{--}8 \text{ m s}^{-1}$ approaching Hawaii. WRF reproduces the QuikSCAT winds in the winter, but slightly underestimates the open ocean wind speed by approximately 0.5 m s^{-1} during the summer months. The seasonal pattern in QuikSCAT also depicts accelerated flows and wakes leeward of the islands, but the wakes are not as prominent as those from WRF likely due to the coarse resolution of 12.5 km. In addition, QuikSCAT is known for overestimation of the wind speed under weak and variable conditions (Pensieri et al., 2010; Satheesan et al., 2007).

The hourly WRF winds with 6 km resolution are interpolated in time and space to match the QuikSCAT data over a 12.5-km grid for computation of the error metrics. Fig. 8 shows the spatial distributions of the mean error, root-mean square error, correlation coefficient, and scatter index of the WRF winds from 2000 to 2009. Kona storms and cold front are less frequent and the error metrics primarily reflect the persistent trade wind conditions in Hawaii. The simulated high-resolution wind data from the WRF model reproduces the approaching flow as well as the local acceleration in the channels and south of Hawaii Island with less than 0.4 m s^{-1} mean error and 2 m s^{-1} root-mean-square error. The corresponding correlation coefficient of 0.7–0.8 and scatter index below 0.2 indicate good agreement between the two datasets in time. The most significant discrepancy occurs in the wake region of Hawaii Island, where the mean and root-mean-square errors reach -2 and 3.8 m s^{-1} , due to overestimation of the wind speed by QuikSCAT. The low correlation and large scatter in the wake region indicate the challenge in modeling of the stochastic processes and remote-detection of the weak, variable flows. Since the fetch is small and the wind speed is low, the wake is not a significant generation region that influences the local wave climate.

The wave conditions in Hawaii are highly localized due to orographically induced airflows as well as sheltering of both the wind waves and swells by the islands. GlobWAVE, which includes altimeters with multiple ground tracks over the Hawaii region, provides a consolidated dataset of significant wave height to assess the spatial pattern of the hindcast. Fig. 9a shows the locations of altimetry observations from 1991 to 2011. The observations adjacent to large landmasses, which have high noise to signal ratio, had been omitted in the dataset. We linearly interpolate the 5.5-km hindcast data in space to match the altimetry record of the nearest hour for comparison. The hindcast and recorded data pairs are binned onto a spatial grid for computation of the error metrics. Fig. 9b shows the grid coverage and the number of data pairs in each bin. The grid resolution of 0.25° is selected to provide an optimal balance between the data density and spatial resolution. The use of multiple platforms over a period of 21 years provides adequate coverage of the waters around the Hawaiian Islands. Bins along tracks of long-running satellites have up to 3410 data pairs, and those with less than 30 data pairs are not considered in the computation of the error metrics.

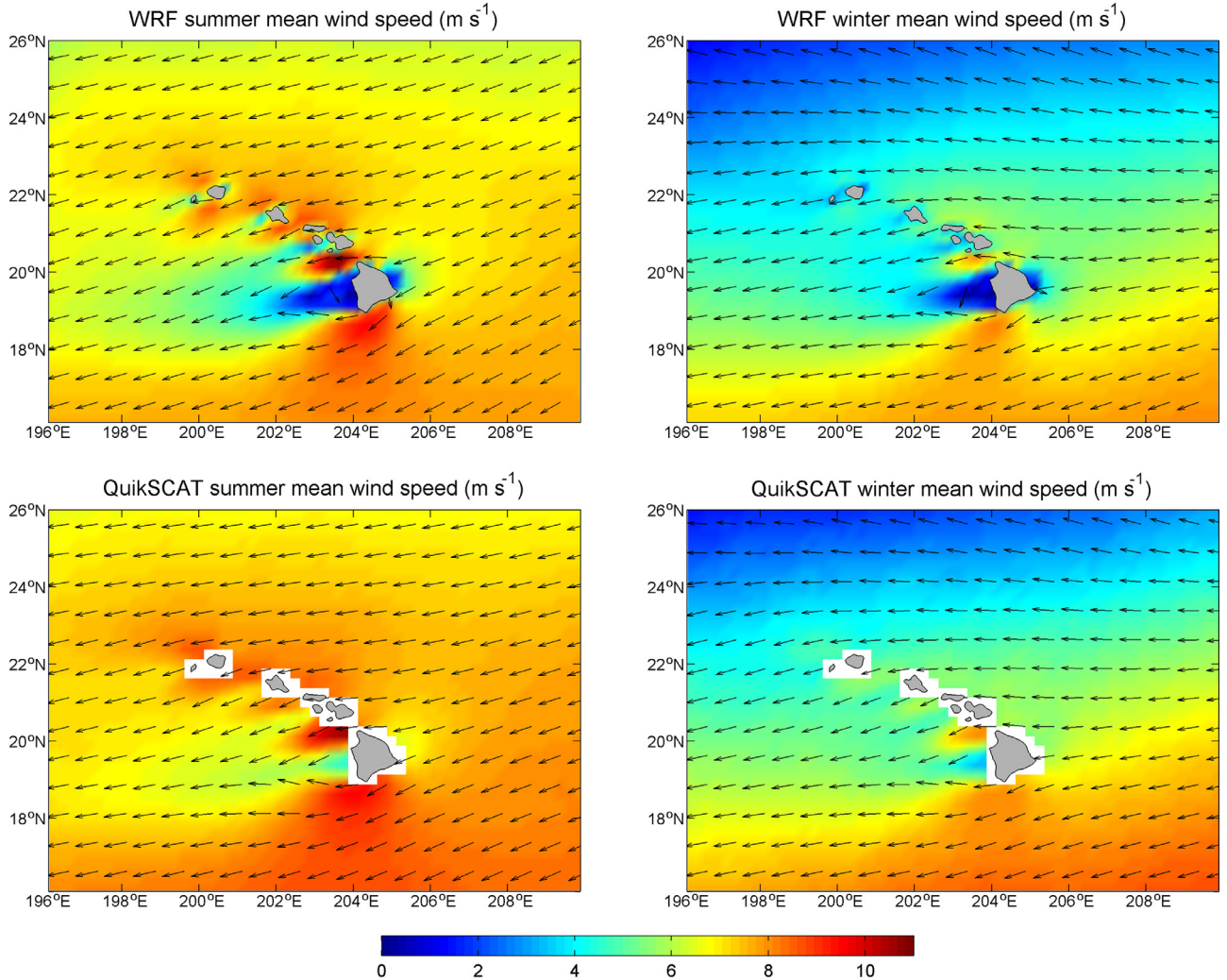


Fig. 7. Mean summer and winter 10-m winds from Hawaii WRF and QuikSCAT for 2000 to 2009.

Fig. 10 shows the mean error, root-mean square error, correlation coefficient, and scatter index to provide an indication of the wave model performance around the Hawaiian Islands. The distribution of the error metrics is influenced by the trade wind waves as well as the north and south swells. Kona storms and cold fronts, which can generate severe wave conditions, are less frequent with negligible influence on the statistics. The mean error shows overestimation of the significant wave height north and south of the island chain and underestimation in the shadows of the northwest swells and trade wind waves. The small error to the southeast of Hawaii Island alludes to accurate reproduction of the trade wind waves. The RMSE follows a similar pattern, but with slightly larger values to the south likely due to the varying shadow region associated with the change of swell direction from northwest to north during the winter season. The high correlation coefficient and low scatter index north and east of the island chain indicate the hindcast captures the timing of the approaching north swell and wind waves reasonably well. The lower correlation and large scatter immediately south and west of the islands reflect the limitation of the spectral models in reproducing the wave conditions in sheltered regions. This is most evident in the region west of Hawaii Island, which is in the shadow of both the northwest swells and trade wind waves.

4.2. Validation with buoy data

The offshore and near-shore buoys around the Hawaiian Islands provide hourly measurements of the wind and wave conditions and several of them were in operation during most of the hindcast period. The detailed in-situ measurements complement the remotely sensed data for validation of the hindcast. [Hitzl et al. \(2014\)](#) validated the simulated high-resolution surface winds from the WRF model with records from 11 offshore and nearshore buoys for 2000 to 2009. The computed speeds have a bias within -0.9 to 0.4 m s^{-1} and RMSE of 1.6 to 3.1 m s^{-1} among the 11 sites during the summer months, when the trade winds are strong and the conditions are challenging to the model. The results are consistent with the QuikSCAT comparison in **Fig. 8**. The highest errors occur at a buoy downstream of Maui and Lanai in the wake of the trade wind flow.

The wave buoys provide the significant wave height and peak period and the recent measurements include the peak direction as well. **Fig. 11** shows, for example, the comparison of the hindcast wave parameters with available measurements at 6 selected offshore and nearshore buoys in 2012 (see **Fig. 1** for location map). The hindcast reproduces the seasonal variations as well as the individual events, albeit the gaps in the records when the buoys were not in operation. Both datasets at the three offshore

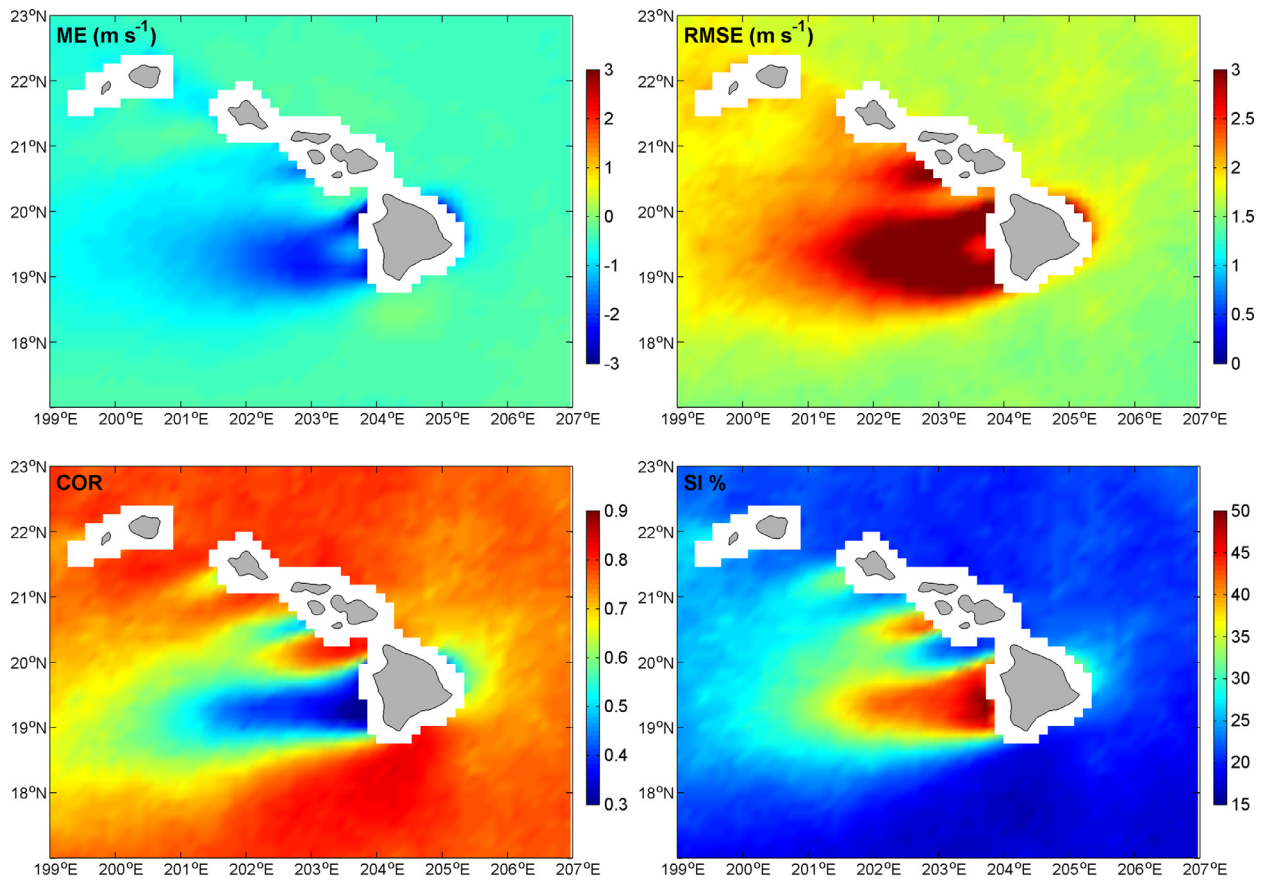


Fig. 8. Error metrics of wind speeds from Hawaii WRF and QuikSCAT for 2000 to 2009.

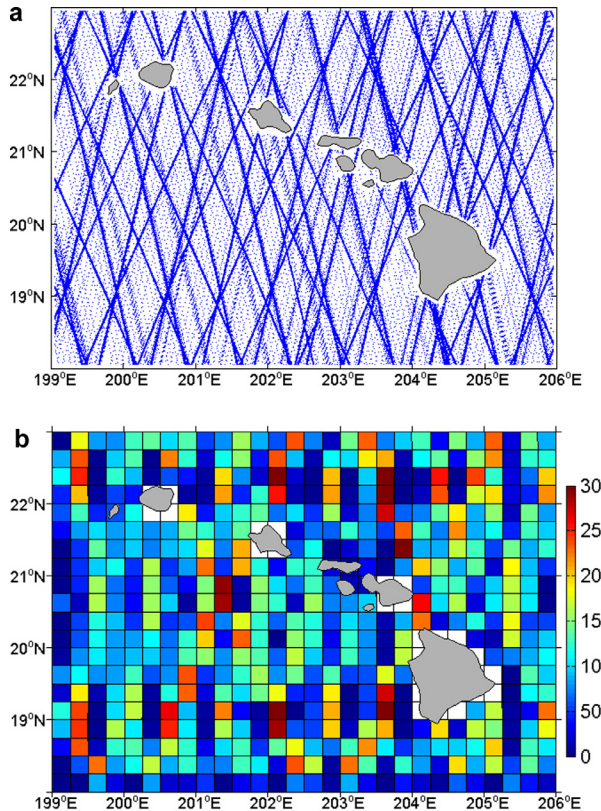


Fig. 9. GlobWAVE altimetry observations around Hawaii from 1991 to 2011.
(a) Track distribution. (b) Number of observations per cell.

buoys indicate persistent east wind waves of 1–3 m significant wave height and 6–10 s peak period around the Hawaiian Islands. The records at buoy #51101 northwest of Kauai also show large north swells reaching 7 m and 21 s in the winter months. The wave height decreases to 5 m at buoy #51002 south of the island chain due to sheltering of the north Pacific swells. Buoy #51004 southeast of Hawaii Island is open to the north, but recorded slightly smaller wave heights because the island chain blocks the more energetic swells from the northwest. Although swells from the South Pacific reach Hawaii all year round, their low energy levels are often masked by the more energetic north swells or wind waves and have little influence on the peak period or direction at the offshore buoys. During the summer, the hindcast shows significant wave heights of over 4.5 m at buoys #51002 and #51004 due to Hurricane Daniel, which only affected the waters south of the island chain.

The records at the three nearshore buoys show distinct wave climate on the north, east, and south sides of Oahu. Buoy #51201 located 9 km off the north shore recorded comparable swell conditions to #51101 with significant wave height and peak period up to 6.3 m and 22 s in the winter. Wind waves of 1 to 2 m height and 5 to 10 s period from the northeast reach the buoy during the summer. Buoy #51202 off the east shore is open to wind waves from the northeast to east, but is partially sheltered from the more energetic northwest swells. The hindcast model reproduces the persistent wind waves of 1–3 m height, but underestimates the intermittent swells, which reach 4.2 m in the records. Buoy #51204 is sheltered from the majority of the north Pacific swells except those passing through Ka'ie'ie Channel from the northwest. The hindcast model resolves the period and direction of the northwest swells reasonably well, but underestimates

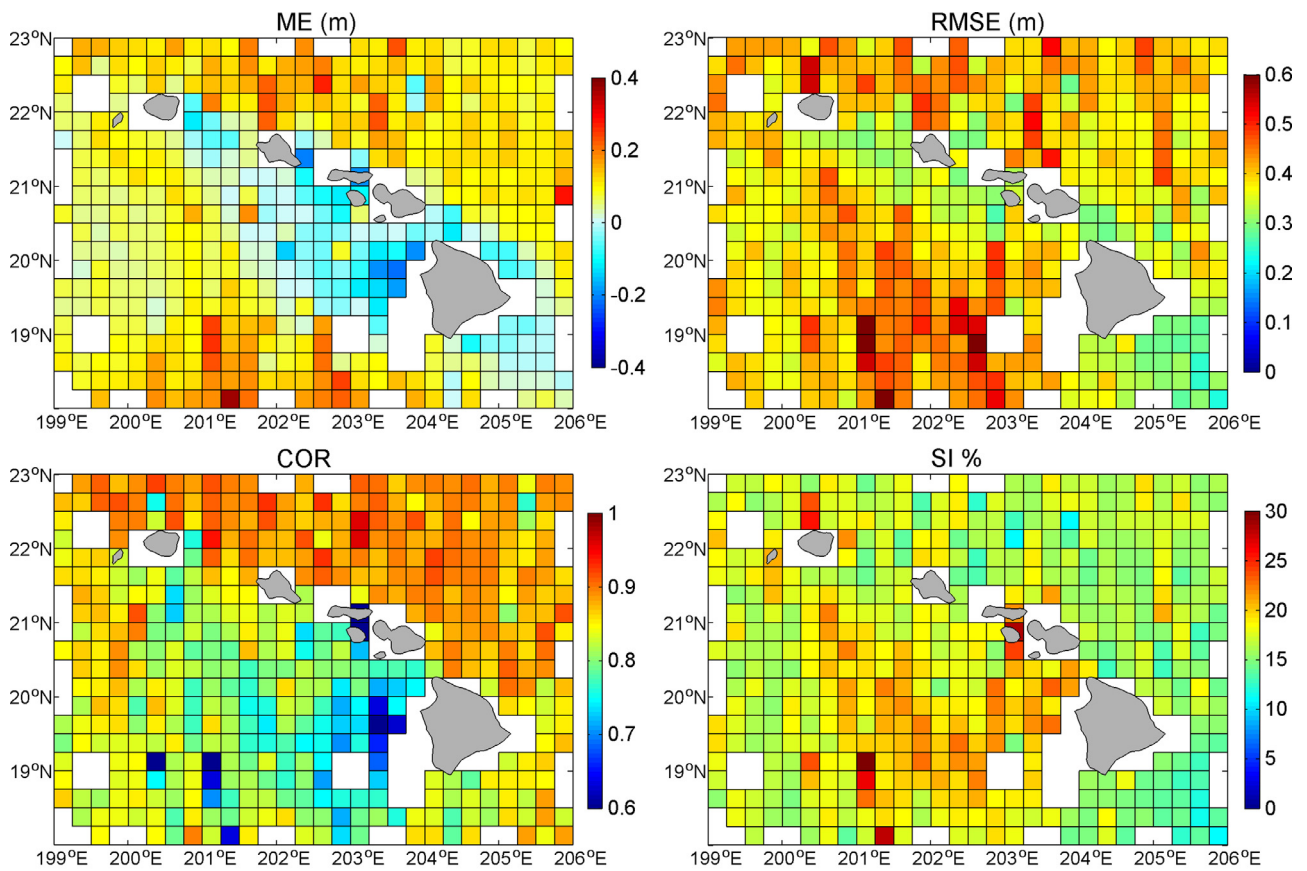


Fig. 10. Error metrics of significant wave heights from Hawaii WAVEWATCH III hindcast and GlobWAVE altimetry measurements for 1991 to 2011.

the height likely due to the low spatial resolution, which cannot fully describe the steep seafloor near the buoy. Since the buoy is sheltered from direct approach of the northeast wind waves during the summer, it recorded clear signals of the south swells with 0.6–1.8 m height and up to 22 s period for validation of the hindcast.

We compile the scatter plots of the hindcast significant wave height against all available buoy data from 1979 to 2013 for an overall assessment. Fig. 12 provides the scatter plots of the two datasets at the six selected buoys. The results at the three offshore buoys demonstrate the model performance in different regions around the island chain. The hindcast predicts the wave height reasonably well with 90% of the data within ± 0.68 m of the records and small RMSEs of 0.29–0.47 m. The apparent large scatter for the energetic events is due to offset of the northwest swell arrivals between the hindcast and buoy measurements. The timing offsets are consistent for the exposed buoys leading to the similar scatter indices of 0.16 and 0.17 at buoys #51101 and buoy #51002 in the northwest and southwest regions. Buoy #51004, sheltered from the northwest swells by the island chain, yields a smaller scatter index of 0.12. Consistent with the altimetry comparison, the mean error at buoys #51101 and 51002 shows a positive bias of 0.16–0.28 m due to the northwest swell. The bias reduces to 0.06 m at buoy #51004 in the shadow of Hawaii Island. The regression lines with slopes of 0.87 to 0.99 and the high correlation coefficients up to 0.91 indicate good overall agreement between the hindcast and recorded wave heights at the offshore locations.

The wave conditions at the nearshore buoys around Oahu are influenced by local island features. Buoy #51201 off the north shore is exposed to northeast wind waves and north Pacific swells and the scatter plot shows a pattern similar to that of the offshore

buoy #51101 with the regression slope close to one. The smaller overall wave height and mean error are due to partial sheltering of the energetic northwest swells by Kauai and the east trade-wind waves by a prominent headland on northeast Oahu. The small RMSE of 0.36 m and the high correlation coefficient of 0.92 indicate good quality of the hindcast at this relatively exposed location. Buoy #51202 off the east shore experiences more gentle wave conditions due to sheltering of the northwest swells by the same headland. While most of the error metrics are comparable to those off the north shore, the ME improves from 0.18 to –0.01 m associated with dominance of the trade wind waves instead of the northwest swells. Buoy #51204 southwest of the island experiences the mildest wave conditions among the three nearshore buoys due to sheltering from the majority of the north Pacific swells and trade wind waves. This buoy is exposed to the year-round south swells with typical significant wave heights of around 1 m. The negative mean error of –0.06 m indicates overall underestimation of the hindcast wave height. The small regression slope of 0.65 implies greater underestimation of the energetic northwest swell events reaching the site. The low correlation of 0.78 is likely due to the limitations of the model in resolving the northwest swells and trade wind waves at this sheltered location.

The Q-Q plots eliminate the timing errors and compare the percentile distributions of the hindcast and recorded significant wave heights. Fig. 13 provides the comparisons at the six selected buoys. The hindcast at the three offshore buoys shows good accuracy for wave heights up to 5 m that account for at least 98% of the occurrence. The model tends to overestimate wave heights above 5 m at the exposed buoys #51101 and 51002, but underestimate at buoy #51004 southeast of Hawaii Island in the shadow of the northwest swells. The extreme wave heights at the two exposed

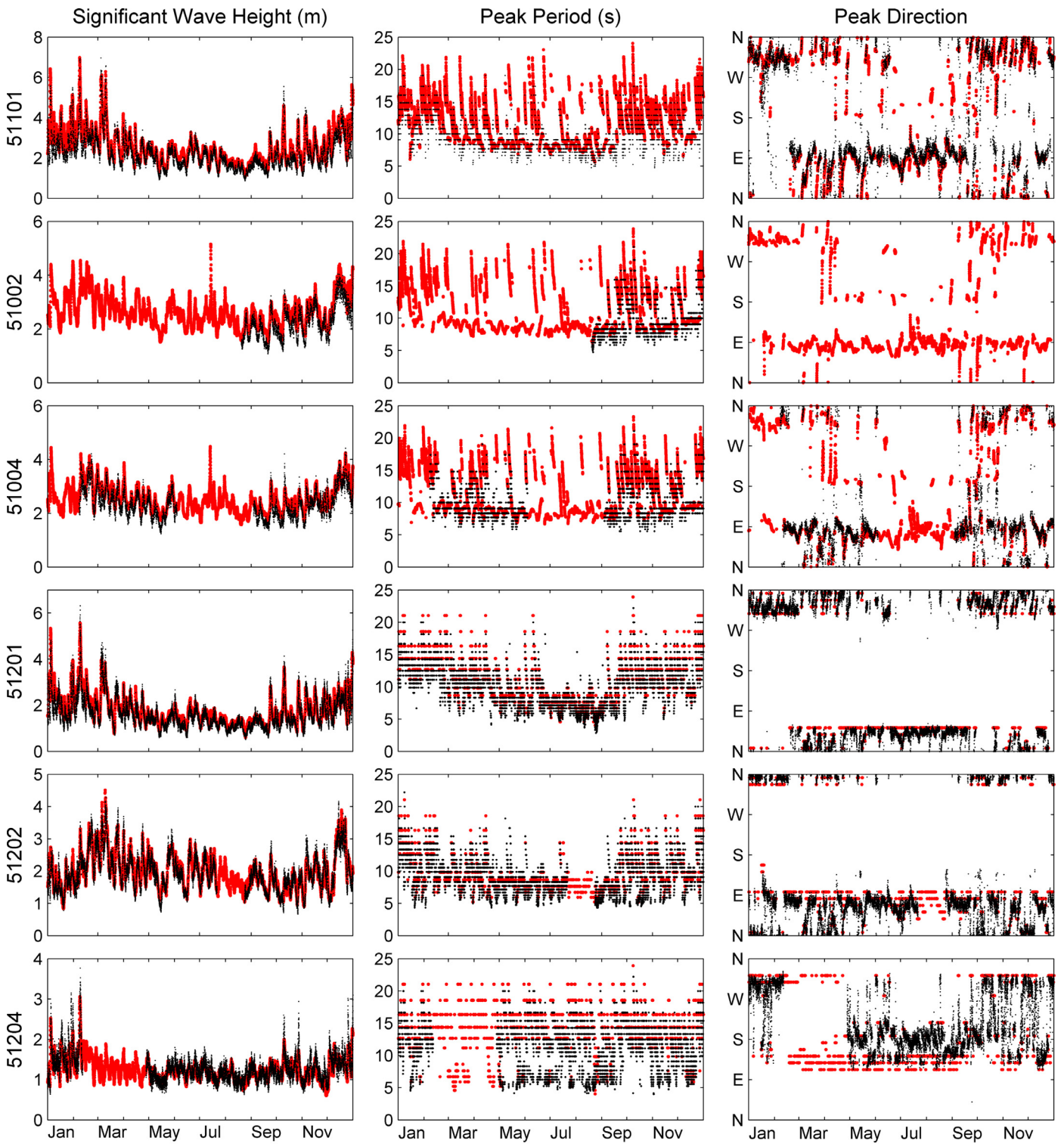


Fig. 11. Comparison of recorded (black) and hindcast (red) wave parameters at selected offshore and nearshore buoys for 2012. (For interpretation of the references to color in this figure legend, the reader is referred to the web version of this article.)

buoys are associated with Kona storms or cold fronts and are well captured by the hindcast due to the proximity of the buoys to the sources. The same pattern also exists at the nearshore buoys around Oahu. The hindcast yields slight overestimates of the wave height at the exposed buoy #51201, but shows underestimation at the sheltered buoys #51202 and 51204 for wave heights above 5 and 1.5 m, which correspond to the 99.6 and 85 % percentiles re-

spectively. The lower predictions of the energetic events at #51202 are due to the model limitations in describing wave transformation around obstacles and in the shadows of islands. The hindcast at buoy #51204 shows underestimation beginning at a smaller wave height and a lower percentile because of its location in the shadows of both the north Pacific swells and northeast trade wind waves.

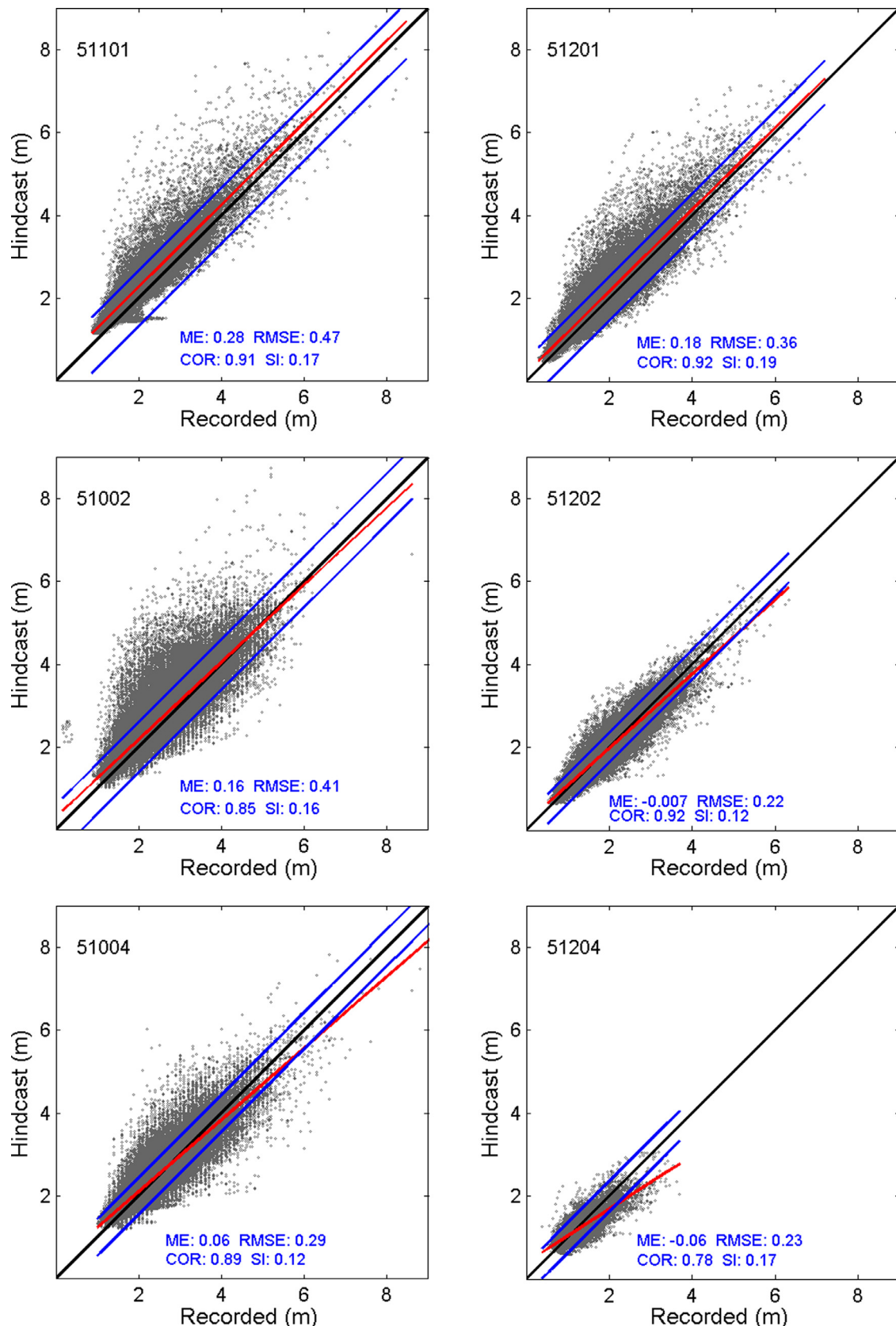


Fig. 12. Scatter plots of hindcast significant wave heights and buoy measurements at selected offshore and nearshore buoys. Black line denotes perfect match, blue lines delineate 90% of the data, and red line is the linear regression. (For interpretation of the references to color in this figure legend, the reader is referred to the web version of this article.)

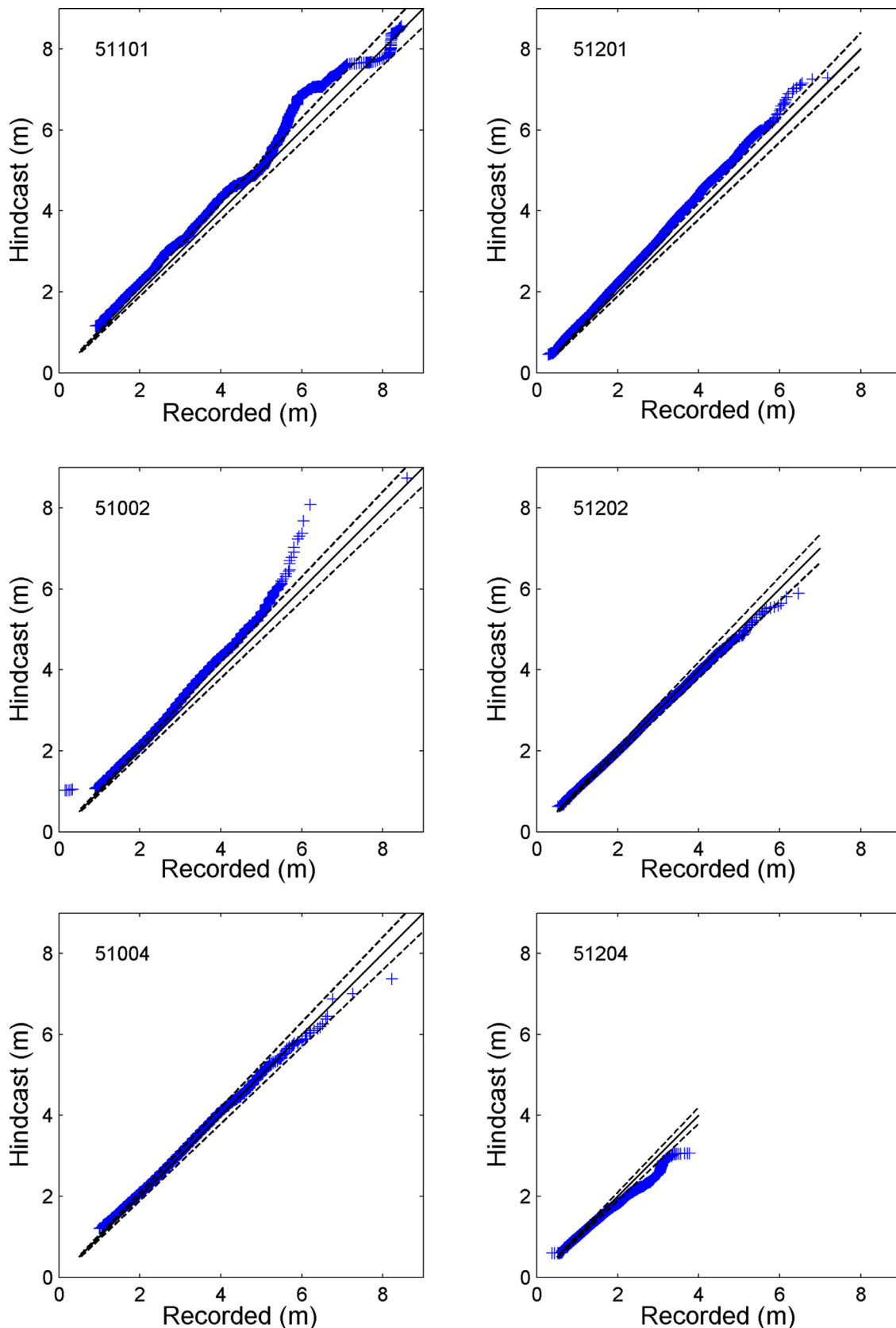


Fig. 13. Quantile-quantile plots of hindcast significant wave heights and buoy measurements at selected offshore and nearshore buoys. Black line denotes perfect match and black dash lines delineate the ±5% error bounds.

Table 3

Error metrics of significant wave height at buoys.

Buoy	Start time	End time	Error bounds ^a (\pm m)	ME (m)	RMSE (m)	COR	SI	Lin. reg. slope
51000	04/23/2009	03/10/2013	0.69	0.27	0.46	0.89	0.16	0.96
51001	02/11/1981	12/24/2009	0.63	0.14	0.44	0.90	0.17	0.95
51002	09/06/1984	01/14/2013	0.61	0.16	0.41	0.85	0.16	0.94
51003	11/01/1984	05/31/2013	0.57	0.10	0.41	0.83	0.18	0.92
51004	11/08/1984	05/31/2013	0.44	0.06	0.29	0.89	0.12	0.87
51100	04/23/2009	05/31/2013	0.65	0.28	0.45	0.90	0.16	0.99
51101	02/21/2008	05/31/2013	0.68	0.28	0.47	0.91	0.17	0.99
51201	09/08/2004	05/31/2013	0.52	0.18	0.35	0.91	0.19	0.96
51202	09/08/2004	05/31/2013	0.35	0.01	0.22	0.92	0.12	0.90
51204	10/13/2010	05/31/2013	0.37	-0.06	0.23	0.78	0.17	0.65
51207	10/29/2012	05/31/2013	0.34	0.02	0.21	0.94	0.12	0.92
KNOH1	09/01/2008	01/18/2012	0.27	-0.07	0.18	0.67	0.23	0.57
39	10/22/1982	09/16/1993	0.90	0.37	0.60	0.87	0.28	1.01
51203	07/01/2007	05/31/2013	0.35	-0.12	0.22	0.71	0.20	0.71
51205	12/05/2011	05/31/2013	0.60	0.21	0.37	0.89	0.15	0.98
51206	03/05/2012	05/31/2013	0.41	-0.01	0.25	0.89	0.12	0.82

^a Error bounds for 90% of the hindcast data from the measurements as illustrated in Fig. 12.**Table 4**

Error metrics of significant wave height from the present and NOAA NCEP hindcasts.

Buoy	Start time	End time	ME (m)		RMSE (m)		COR		SI		Lin. reg. slope	
			NOAA	Present	NOAA	Present	NOAA	Present	NOAA	Present	NOAA	Present
51001	02/11/1981	12/31/2007	0.24	0.14	0.49	0.44	0.91	0.90	0.18	0.17	1.05	0.95
51002	09/06/1984	12/31/2007	0.21	0.14	0.45	0.40	0.86	0.85	0.16	0.16	1.04	0.94
51003	11/01/1984	12/31/2007	0.13	0.07	0.42	0.39	0.86	0.85	0.18	0.17	1.07	0.96
51004	11/08/1984	12/31/2007	0.15	0.04	0.34	0.29	0.89	0.89	0.13	0.12	0.99	0.87

The time series, scatter, and Q–Q plots from the six selected buoys have illustrated the relationships between the hindcast and recorded datasets at the regional and island scales. Table 3 summarizes the error metrics from the 16 buoys based on all available measurements (see Fig. 1 for location map). Ninety percent of the hindcast wave heights are within ± 0.69 m or less of the measurements, except for buoy #39, which only recorded episodic events. The mean error at the offshore buoys #51000, 51001, 51003, 51100, and 51101 and the nearshore buoys #39, 51201 and 51205, which are exposed to north Pacific swells, shows a consistent positive bias of 0.10 to 0.37 m. Buoy #51002 south of the island chain is sheltered from the late season north swells. Its comparable ME of 0.16 m implies the consistent positive bias comes from the more energetic and frequent northwest swells. The offshore buoy #51004 and the nearshore buoys #51202, 51207, and 51206, which are partially sheltered from the northwest swells, show negligible or small MEs of -0.01 to 0.06 m. The nearshore buoys KNOH1, #51203, and 51204, which are at well-sheltered locations from the north Pacific swells and northeast trade wind waves, show negative biases of -0.06 to -0.12 and low correlation coefficients of 0.67–0.78. The hindcast at these locations also shows strong tendency to underestimate the large events as indicated by the 0.57–0.71 regression slopes. The errors likely arise from the relatively low resolution of 500 m close to the shore and limitations of the spectral model in resolving the transformation of the dominant wave events into the shadow areas.

4.3. Comparison with previous and existing hindcast datasets

The present hindcast utilizes the updated source-term package from Arduin et al. (2010) and the CFSR winds with high-resolution WRF data around Hawaii. We have already demonstrated the role of the high-resolution winds in the local wave field. A comparison with selected previous and existing datasets can infer the added values of the source term package and CFSR. Table 4 compares the error metrics computed for the present

dataset and the NOAA NCEP WAVEWATCH III hindcast of Chawla et al. (2013) at four offshore buoys around Hawaii. The comparison makes use of available buoy records during the span of the NOAA hindcast from 1979 to 2007. The NOAA hindcast utilized the CFSR wind forcing and the source term package of Tolman and Chalikov (1996), which is known to underestimate the dissipation and overestimate the swell energy (Hanson et al., 2009; Stopa et al., 2015). The present hindcast shows comparable correlation coefficients and scatter indices due to the use of the same wind forcing. For the comparable offshore resolution, the consistent reduction of the positive bias, RMSE, and the regression slope points to improvement of the generation and dissipation mechanisms in the source term of Arduin et al. (2010).

Table 5 compares the error metrics from the present study with the previous hindcast of Stopa et al. (2013), which used the source term of Tolman and Chalikov (1996) and the lower resolution FNL global winds. The high-resolution computations with WRF wind forcing around the Hawaiian Islands in both studies allow direct comparison of the hindcast datasets at the near-shore buoys. The error metrics are recomputed at the buoys considered in the earlier hindcast using available measurements from 2000 to 2009. The present hindcast shows consistent improvement in terms of the RMSE, correlation coefficient, and scatter index. This is reflected in the accurate description of the individual events from the CFSR winds as illustrated in the time series comparison in Fig. 11. The two datasets have comparable positive bias at buoys open to the north Pacific swells despite the lower dissipation in the source term used in the previous study. Furthermore, the present hindcast has higher linear regression slopes closer to one. This alludes to the underestimation of the wind forcing from FNL and highlights the improvement of CFSR in describing the more severe events as pointed out by Stopa and Cheung (2014).

The positive bias of the swell prediction is still present with the source term of Arduin et al. (2010) and is a topic of on-going investigation (Stopa et al., 2015). On the other hand, the present hindcast tends to give negative bias at sheltered locations as shown

Table 5

Error metrics of significant wave height from the present hindcast and the prior work of Stopa et al. (2013).

Buoy	Start time	End time	ME (m)		RMSE (m)		COR		SI		Lin. Reg. slope	
			Prior	Present	Prior	Present	Prior	Present	Prior	Present	Prior	Present
51001	01/02/2000	12/24/2009	0.08	0.14	0.38	0.39	0.90	0.91	0.16	0.16	0.83	0.95
51002	01/02/2000	12/31/2009	0.11	0.16	0.39	0.36	0.80	0.87	0.15	0.14	0.81	0.93
51003	01/02/2000	12/31/2009	0.1	0.06	0.38	0.33	0.81	0.86	0.17	0.15	0.82	0.93
51004	01/02/2000	10/07/2009	0.02	0.06	0.29	0.24	0.87	0.91	0.12	0.10	0.75	0.85
51100	04/24/2009	12/31/2009	0.26	0.20	0.44	0.35	0.89	0.92	0.16	0.14	0.88	0.90
51101	02/21/2008	12/31/2009	0.26	0.24	0.49	0.46	0.88	0.90	0.19	0.18	0.82	0.93
51201	09/08/2004	12/31/2009	0.09	0.17	0.35	0.35	0.90	0.92	0.2	0.19	0.92	0.96
51202	09/08/2004	12/30/2009	0.09	-0.01	0.29	0.23	0.89	0.92	0.14	0.12	0.86	0.88
51203	07/01/2007	12/31/2009	0.11	-0.13	0.26	0.22	0.67	0.76	0.27	0.20	0.70	0.73
KNOH1	09/01/2008	12/31/2009	0.09	-0.07	0.23	0.18	0.59	0.68	0.28	0.23	0.60	0.56

in Table 3 and Fig. 10 despite the overestimation of the approaching swells. This is likely attributed to the absence of diffraction in the governing equation used by the spectral wave models. As part of a sensitivity study prior to the production runs, we conducted a series of numerical experiments with the approximate diffraction scheme in the Oahu SWAN model and did not obtain noticeable improvement of the results at buoy #51204 in the shadows of the north swells and the trade wind waves. Further development and calibration of the diffraction scheme are needed to account for the energy transfer into the sheltered region behind a massive headland or island.

5. Conclusions

A system of nested mesoscale atmospheric and spectral wave models driven by the Climate Forecast System Reanalysis (CFSR) has produced high-resolution regional wind and wave data from 1979 to 2013. The 34-year dataset provides a wealth of information for climate research, infrastructure planning, and resources assessment in Hawaii. The use of CFSR and the updated source term in WAVEWATCH III provides improved description of the ocean waves in comparison to previous and existing hindcasts. The high-resolution computations capture unique features of the regional wind and wave fields along the Hawaiian Islands. The multi-modal sea states include waves generated by trade winds, cold fronts, and Kona storms as well as swells from north and south Pacific extratropical storms. Comprehensive satellite and buoy measurements allow validation of the hindcast for practical application and examination of model performance in the challenging environment of Hawaii.

The QuikSCAT and buoy measurements from 2000 to 2009 provide assessment of the spatial and temporary patterns of the regional wind hindcast. The computed wind data captures the year-round trade winds as well as episodic cold fronts and Kona storms in Hawaii. The persistent trade winds from the east and northeast dominate the orographically induced airflows that include deceleration on the windward slopes, acceleration in channels and around southern Hawaii Island, and prominent wake formation leeward of the islands. Comparison with QuikSCAT wind fields shows good overall agreement of the seasonal variation of the trade wind flow as well as its local deceleration and acceleration around the islands. Discrepancies primarily occur in the wake regions leeward of the islands due to inadequate spatial resolution of QuikSCAT and its overestimation under calm and variable conditions. The cold fronts and Kona storms are rapidly varying systems passing through the islands within a period of several days. Comparison with the measurements shows good reproduction of the general flow patterns and timing of the events.

The wave climate in Hawaii is dominated by trade wind waves and north Pacific swells. The south swells, despite their year-

around occurrence, are typically small and masked by the dominant wave components. Cold fronts and Kona storms are less frequent, but can generate severe wave conditions. The altimetry observations provide validation of the spatial patterns of selected events corresponding to these wave regimes. The long-term comparison of the hindcast with available buoy measurements from 1979 to 2013 and altimetry measurements from 1991 to 2011 primarily reflects the dominant trade wind waves and north Pacific swells. The hindcast provides a good description of the trade wind waves but tends to overestimate the energetic northwest swells. The spectral models, however, underestimate the wave height in the shadows of both the wind waves and swells. Accurate modeling of the wave fields at sheltered locations requires diffraction and other energy transfer mechanisms in the model. The comparison with the recorded data validates the 34-year hindcast dataset and identifies limitations of spectral wave modeling. In addition to climate research and engineering application, the hindcast dataset provides a baseline for future model development and parameterization especially for island environments.

Acknowledgments

The Department of Energy is the primary sponsor for the development of the hindcast dataset with funding through grant no. DE-FG36-08GO18180 via the Hawaii National Marine Renewable Energy Center. The Department of Navy provided additional support through Task Order No. N00024-08-D-6323 via Applied Research Laboratory at the University of Hawaii. SOEST Contribution Number 9576.

References

- Ardhuin, F., Rogers, E., Babanin, A., Filipot, J.-F., Magne, R., Roland, A., van der Westhuysen, A., Queffoulou, P., Lefevre, J.-M., Aouf, L., Collard, F., 2010. Semi-empirical dissipation source functions for ocean waves. Part I: Definition, calibration, and validation. *J. Phys. Oceanogr.* 40 (9), 1917–1941.
- Arinaga, R.A., Cheung, K.F., 2012. Atlas of global wave energy from 10 years of reanalysis and hindcast data. *Renewable Energy* 39 (1), 49–64.
- Aucan, J.P., 2006. Directional wave climatology for the Hawaiian Islands from buoy data and the influence of ENSO on extreme wave events from wave model hindcast. In: Proceedings of the 9th International Workshop on Wave Hindcasting and Forecasting. Victoria, British Columbia.
- Banner, M.L., Morison, R.P., 2010. Refined source terms in wind wave models with explicit wave breaking prediction. Part I: assessment of existing model performance. *Ocean Modell.* 33 (1–2), 177–189.
- Bidlot, J., Janssen, P., Abdalla, S., 2007. A revised formulation for ocean wave dissipation and its model impact. ECMWF Technical Memorandum 509, Reading, UK.
- Boisséson, E., Balmaseda, M.A., Abdalla, S., Källén, E., Janssen, P.A.E.M., 2014. How robust is the recent strengthening of the Tropical Pacific trade winds? *Geophys. Res. Lett.* 41 (12), 4398–4405.
- Booij, N., Ris, R.C., Holthuijsen, L.H., 1999. A third-generation wave model for coastal regions. Part I, model description and validation. *J. Geophys. Res.* 104 (C4), 7649–7666.
- Caires, S., Sterl, A., Bidlot, J.-R., Graham, N., Swail, V., 2004. Intercomparison of different wind-wave reanalysis. *J. Clim.* 17 (10), 1893–1913.

- Caldwell, P.C., Vitousek, S., Aucan, J.P., 2009. Frequency and duration of coinciding high surf and tides along the north shore of Oahu, Hawaii. *J. Coastal Res.* 25 (3), 734–743.
- Carlis, D.L., Chen, Y.-L., Morris, V.R., 2010. Numerical simulations of island-scale airflow over Maui and the Maui vortex during summer trade-wind conditions. *Mon. Weather Rev.* 138 (7), 2706–2736.
- Caruso, S.J., Businger, S., 2006. Subtropical cyclogenesis over the central north Pacific. *Weather Forecasting* 21 (2), 193–205.
- Chawla, A., Spindler, D.M., Tolman, H.L., 2013. Validation of a thirty year reanalysis using climate forecast system reanalysis winds. *Ocean Modell.* 70, 189–206.
- Cheung, K.F., Bai, Y., Yamazaki, Y., 2013. Surges around the Hawaiian Islands from the 2011 Tohoku tsunami. *J. Geophys. Res. Oceans* 118 (10), 5703–5719.
- Dee, D.P., Uppala, S.M., Simmons, A.J., Berrisford, P., Poli, P., Kobayashi, S., Andrae, U., Balmaseda, M.A., Balsamo, G., Bauer, P., Bechtold, P., Beljaars, A.C.M., van der Berg, L., Bidlot, J., Bormann, N., Delsol, C., Dragani, R., Fuentes, M., Geer, A.J., Haimesberger, L., Healy, S.B., Hersbach, H., Hölm, E.V., Isaksen, L., Källberg, P., Köhler, M., Matricardi, M., McNally, A.P., Monge-Sanz, B.M., Morcrette, J.-J., Park, B.-K., Peubey, C., de Rosnay, P., Tavolato, C., Thépaut, J.-N., Vitart, F., 2011. The ERA-Interim reanalysis: configuration and performance of the data assimilation system. *Q. J. R. Meteorol. Soc.* 137 (656), 553–597.
- Ebuchi, N., Gruber, H.C., Caruso, M.J., 2002. Evaluation of wind vectors observed by QuikSCAT/SeaWinds using ocean buoy data. *J. Atmos. Oceanic Technol.* 19 (12), 2049–2062.
- Ek, M.B., Mitchell, K.E., Lin, Y., Rogers, E., Grunmann, P., Koren, V., Gayno, G., Tarpley, J.D., 2003. Implementation of Noah land surface model advances in the National Centers for Environmental Prediction operational mesoscale Eta model. *J. Geophys. Res. Atmos.* (1984–2012) 108 (D22). doi:10.1029/2002JD003296.
- Filipot, J.-F., Cheung, K.F., 2012. Spectral wave modeling for fringing reef environment. *Coastal Eng.* 67, 67–79.
- Foster, J., Li, N., Cheung, K.F., 2014. Sea state determination from ship-based geodetic GPS. *J. Atmos. Oceanic Technol.* 31 (11), 2556–2564.
- Fyfe, J.C., 2003. Extratropical southern hemisphere cyclones: harbingers of climate change? *J. Clim.* 16 (17), 2802–2805.
- Garza, J.A., Chu, P.S., Norton, C.W., Schroeder, T.A., 2012. Changes of the prevailing trade winds over the islands of Hawaii and the North Pacific. *J. Geophys. Res. Atmos.* (1984–2012) 117 (D11). doi:10.1029/2011JD016888.
- Grimmies, S.M., Harrison, M.J., Pacanowski, R.C., Rosati, A., 2004. Technical Guide to MOM4. GFDL Ocean Group Technical Report No. 5, Princeton, New Jersey, 337 pp.
- Hanson, J.L., Tracy, B.A., Tolman, H.L., Scott, R.D., 2009. Pacific hindcast performance of three numerical wave models. *J. Atmos. Oceanic Technol.* 26 (8), 1614–1633.
- Hitzl, D.E., Chen, Y.-L., Nguyen, H.V., 2014. Numerical simulations and observations of airflow through the 'Alenuihaha Channel, Hawaii. *Mon. Weather Rev.* 142 (12), 4696–4718.
- JPL, 2000. QuikSCAT Science Data Product User's Manual. Jet Propulsion Laboratory Publication, Pasadena, California, p. 84.
- Leckler, F., Arduin, F., Filipot, J.-F., Mironov, A., 2013. Dissipation source terms and whitecap statistics. *Ocean Modell.* 70 (9), 62–74.
- Li, N., Roeber, V., Yamazaki, Y., Heitmann, T.W., Bai, Y., Cheung, K.F., 2014. Integration of coastal inundation modeling from storm tides to individual waves. *Ocean Modell.* 83, 26–42.
- McPhaden, M.J., Zebiak, S.E., Glantz, M.H., 2006. ENSO as an integrating concept in earth science. *Science* 314 (5806), 1740–1745.
- Nguyen, H.V., Chen, Y.-L., Fujioka, F., 2010. Numerical simulations of island effects on airflow and weather during the summer over the Island of Oahu. *Mon. Weather Rev.* 138 (6), 2253–2280.
- O'Connor, C.F., Chu, P.S., Hsu, P.C., Kodama, K., 2015. Variability of Hawaiian winter rainfall during La Niña events since 1956. *J. Clim.* 28 (19), 7809–7823.
- Otkin, J.A., Martin, J.E., 2004. A synoptic climatology of the subtropical Kona Storm. *Mon. Weather Rev.* 132 (6), 1502–1517.
- Pensiero, S., Bozzano, R., Schiano, M.E., 2010. Comparison between QuikSCAT and buoy wind data in the Ligurian Sea. *J. Mar. Syst.* 81 (4), 286–296.
- Ponce de Leon, S., Guedes Soares, C., 2005. On the sheltering effects of islands in ocean wave models. *J. Geophys. Res. Ocean* 110 (C9), 2156–2202.
- Quefférou, P., Croizé-Fillon, D., 2010. Global Altimeter SWH Data Set, Version 7, May 2010 Technical Report, Ifremer, France. ([ftp://ftp.fremer.fr/ifremer/cersat/products/swath/altimeters/waves/documentation/altimeterwavermerge7.0.pdf](http://ftp.fremer.fr/ifremer/cersat/products/swath/altimeters/waves/documentation/altimeterwavermerge7.0.pdf)).
- Raschke, N., Arduin, F., 2013. A global wave parameter database for geophysical applications. Part 2: model validation with improved source term parameterization. *Ocean Modell.* 70, 174–188.
- Rogers, W.E., Babanin, A.V., Wang, D.W., 2012. Observation-consistent input and whitecapping dissipation in a model for wind-generated surface waves: description and simple calculations. *J. Atmos. Oceanic Technol.* 29 (9), 1329–1346.
- Saha, S., Moorthi, S., Pan, H.L., Wu, X., Wang, J., Nadiga, S., Tripp, P., Kistler, R., Woolen, J., Behringer, D., Liu, H., Stokes, D., Grumbine, R., Gayno, G., Wang, J., Hou, Y.T., Chuang, H., Juang, H.M.J., Sela, J., Iredell, M., Treadon, R., Klesits, D., Felst, P.V., Keyser, D., Derber, J., Ek, M., Meng, J., Wei, H., Yang, R., Lord, S., van den Dool, H., Kumar, A., Wang, W., Long, C., Chelliah, M., Xue, Y., Huang, B., Schemm, J., Ebisuzaki, W., Lin, R., Xie, P.P., Chen, M., Zhou, S., Higgins, W., Zou, C.Z., Liu, Q., Chen, Y., Han, Y., Cucurull, L., Reynolds, R.W., Rutledge, G., Goldberg, M., 2010. The NCEP climate forecast system reanalysis. *Bull. Am. Meteorol. Soc.* 91 (7), 1015–1057.
- Saha, S., Moorthi, S., Wu, X., Wang, J., Nadiga, S., Tripp, P., Behringer, D., Hou, Y.T., Chuang, H., Iredell, M., Ek, M., Meng, J., Yang, R., Mendez, M.P., Dool, H., Zhang, Q., Wang, W., Chen, M., Becker, E., 2014. The NCEP climate forecast system version 2. *J. Clim.* 27 (6), 2185–2208.
- Satheesan, K., Sarkar, A., Parekh, A., RameshKumar, M.R., Kuroda, Y., 2007. Comparison of wind data from QuikSCAT and buoys in the Indian Ocean. *Int. J. Remote Sens.* 28 (10), 2375–2382.
- Simpson, R.H., 1952. Evolution of the Kona storm a subtropical cyclone. *J. Meteorol.* 9 (1), 24–35.
- Skamarock, W.C., Klemp, J.B., 2008. A time-split nonhydrostatic atmospheric model for weather and forecasting applications. *J. Comput. Phys.* 227 (7), 3465–3485.
- Stopa, J.E., Arduin, F., Babanin, A.V., Zieger, S., 2015. Comparison and validation of physical wave parameterizations in spectral wave models. *Ocean Modell.* doi:10.1016/j.ocemod.2015.09.003.
- Stopa, J.E., Cheung, K.F., 2014. Periodicity and patterns of ocean wind and wave climate. *J. Geophys. Res. Oceans* 119 (8), 5563–5584.
- Stopa, J.E., Cheung, K.F., Chen, Y.-L., 2011. Assessment of wave energy resources in Hawaii. *Renewable Energy* 36 (2), 554–567.
- Stopa, J.E., Filipot, J.-F., Li, N., Cheung, K.F., Chen, Y.-L., Vega, L., 2013. Wave energy resources along the Hawaiian Islands chain. *Renewable Energy* 55, 305–321.
- Stopa, J.E., Cheung, K.F., Tolman, H.L., Chawla, A., 2013. Patterns and cycles in the climate forecast system reanalysis wind and wave data. *Ocean Modell.* 70, 207–220.
- Stopa, J.E., Cheung, K.F., 2014. Intercomparison of wind and wave data from the ECMWF reanalysis interim and NCEP climate forecast system reanalysis. *Ocean Modell.* 75, 65–83.
- Tu, C.-C., Chen, Y.-L., 2011. Favorable conditions for the development of a heavy rainfall event over Oahu during the 2006 wet period. *Weather Forecasting* 26 (3), 280–300.
- Tolman, H.L., 2008. A mosaic approach to wind wave modeling. *Ocean Modell.* 25, 35–47.
- Tolman, H.L., Banner, M.L., Kaihatu, J.M., 2013. The NOPP operational wave model improvement project. *Ocean Modell.* 70, 2–10.
- Tolman, H.L., Chalikov, D., 1996. Source terms in a third-generation wind wave model. *J. Phys. Oceanogr.* 26 (2), 2497–2518.
- Tolman, H.L., and the WAVEWATCH III ® Development Group. 2014. User Manual and System Documentation of WAVEWATCH III® version 4.18. Technical Note 316, NOAA/NWS/NCEP/MMAB, 282 pp.+ Appendices.
- Van der Westhuysen, A.J., 2007. Advances in the Spectral Modelling of Wind waves in the Nearshore (Ph.D. thesis). Delft University of Technology, the Netherlands.
- Van der Westhuysen, A.J., Zijlema, M., Battjes, J.A., 2007. Nonlinear saturation based whitecapping dissipation in SWAN for deep and shallow water. *Coastal Eng.* 54 (2), 151–170.
- Yang, F., Pan, H.L., Krueger, S.K., Moorthi, S., Lord, S.J., 2006. Evaluation of the NCEP global forecast system at the ARM SGP site. *Mon. Weather Rev.* 134 (12), 3668–3690.
- Yang, Y., Chen, Y.-L., Fujioka, F.M., 2005. Numerical simulations of the island-induced circulation over the island of Hawaii during HaRP. *Mon. Weather Rev.* 133 (12), 3693–3713.
- Yin, J.H., 2005. A consistent poleward shift of the storm tracks in simulations of 21st century climate. *Geophys. Res. Lett.* 32 (18). doi:10.1029/2005GL023684.
- Zhang, Y., Chen, Y.-L., Schroeder, T.A., Kodama, K., 2005. Numerical simulations of sea breeze circulations over northwest Hawaii. *Weather Forecasting* 20 (6), 827–846.
- Zhou, C., Chen, Y.-L., 2014. Assimilation of GPS RO refractivity data and its impact on simulations of trade wind inversion and a winter cold front in Hawaii. *Nat. Sci.* 6 (8), 605–614.
- Zieger, S., Babanin, A.V., Rogers, W.E., Young, I.R., 2015. Observation-based source terms in the third-generation wave model WAVEWATCH. *Ocean Modell.* 96 (1), 2–25.
- Zieger, S., Vinoth, J., Young, I.R., 2009. Joint calibration of multi-platform altimeter measurements of wind speed and wave height over the past 20 years. *J. Atmos. Oceanic Technol.* 26 (12), 2549–2564.